First-principles study of interaction energies of atomic defects in bcc ferromagnetic iron

E. Akshaya Devi, Ravi Chinnappan,* and C. S. Sundar
Materials Science Group, Indira Gandhi Centre for Atomic Research, HBNI, Kalpakkam 603102, Tamilnadu, India

(Received 4 October 2017; revised manuscript received 26 March 2018; published 4 October 2018)

A comprehensive calculation of the solute formation energies, solute-solute and vacancy-solute binding energies in bcc iron is reported. An extended set of solutes with atomic numbers 1 to 54 has been considered. We used the projector augmented wave method of density functional theory with the generalized gradient approximation for the exchange-correlation energy functional. The prominent results are the following: (1) formation energies of solutes from fourth and fifth periods vary with their atomic numbers such that they reach maxima near the ends of the periods and a minimum in between, with a local increase near Cu and Ag (like a quasiparabolic valley). Solutes from second and third periods show similar trend like the elements near the ends of the fourth and fifth periods. (2) The size factors of the solutes also show similar variation with their atomic numbers like their formation energies. These trends corroborate the relatively smaller formation energies and size factors of the common alloying additions to Fe (such as $3d$, $4d$, and sp elements) as compared to solutes that lack solubility (such as Li, Na, K, Rb, He, Ne, Ar, Kr, Xe, F, Cl, Br, I, Mg, Ca, Sr, Ag, Cd, In, Y). (3) The solubilities estimated from our formation energies are found to be in reasonable agreement with those from the phase diagram database. (4) Solute-solute and vacancy-solute binding energies are found to vary with the atomic number of the solutes in a manner inverse to solute formation energies and solute size factors, reaching strong binding energies near the ends of the periods which generally include the insoluble elements. (5) Another trend revealed by our work is that the size factors of isoelectronic sets of solutes increase down the groups with associated increase of formation energies, and strength of solute-solute and vacancy-solute binding energies. (6) A significant correlation is found between our vacancy-solute binding energies of $3d$ and $4d$ elements and the corresponding diffusion coefficients from literature whereby solutes with strong binding energies have higher diffusion coefficients and vice versa.

DOI: 10.1103/PhysRevB.98.144104

I. INTRODUCTION

In nuclear power plants, stainless steels are the predominant structural materials. Ferritic and ferritic-martensitic steels are known to offer better dimensional stability than austenitic steels under neutron irradiation. The operating temperatures of these steels are however limited to about 600 °C. In order to achieve higher operating temperatures, oxide dispersion strengthened (ODS) steels have been developed [1,2]. These modern steels are multicomponent alloys (with about 20 components [2]: Fe, C, Mn, P, Si, Ni, Cr, Mo, V, Ti, Co, Cu, Al, B, W, Zr, N, O, Y) made up of Fe-Cr ferrite matrix in which a homogeneous distribution of small precipitate particles is created by ball milling and subsequent consolidation process involving either hot extrusion or hot isostatic pressing. These ODS steels have superior creep resistance and stability under irradiation, attributed to the finest oxide particles densely dispersed in the ferrite matrix with high dislocation density. These nanoprecipitates have been the subject of many characterization studies. They are found to be extremely stable even at high temperatures close to the solidus of the ferrite matrix. Stability of the microstructure of these steels under irradiation is also important for their long-term service in nuclear environment. Some experimental studies suggest that the nanoparticles are stable under irradiation but other studies report their dissolution. Thus the evolution of size and population of these dispersed nanoparticles is not well understood [3].

Formation of precipitates is governed by diffusion kinetics of solute atoms in the solvent matrix. Vacancy and solute formation energies and solute-solute and vacancy-solute binding energies are important parameters controlling the diffusion of solute atoms hence nucleation, growth, and coarsening of precipitates [4–9]. First-principles electronic structure calculations offer the most accurate means to develop an atomic level understanding of the interactions of solutes and point defects in solids [4,10]. Modeling of clustering of atomic defects and swelling also suggests that accurate characterization of the interactions of solutes with point defects is important [10–16]. Fu *et al.* have shown that the unusually high solubility of oxygen atoms and nucleation of stable oxygen-enriched nanoparticles in defect-containing Fe is determined by the formation and binding energies of vacancies, oxygen, and other solutes present in iron [17].

Given these connections between formation and binding energies of atomic defects and diffusion kinetics and hence evolution of microstructure and mechanical properties of steels, several researchers have studied the interactions of solute elements with point defects in body-centered cubic (bcc) iron employing first-principles computational methods [18–20] based on the electronic density functional theory

*ravic@igcar.gov.in

(DFT). These studies have however considered mainly transition metals and *sp* elements. Further, the specifications of the DFT calculations employed in previous works on this topic are not consistent among themselves. Olsson *et al.* and You *et al.* have carried out their electronic structure calculations under constant volume conditions [18,20]. Gorbatov *et al.* have done the calculations by Green function method with atomic sphere approximation which preclude relaxation of ionic coordinates. They themselves have indicated that the vacancy-solute binding energies of certain solutes (Sc, Ti, Mo) are extremely sensitive to the extent of structural relaxation included in the calculations [19]. Partly relaxed or un-relaxed calculations can thus give different results [21–25].

We in this work go beyond the set of solute elements considered in the previous works and make a large database of predictions of solute formation energies, solute-solute, and vacancy-solute binding energies for an extended set of 53 different solute elements, with atomic numbers 1 to 54, in bcc ferromagnetic iron using DFT total energy calculations with complete relaxation of structural degrees of freedom (ionic coordinates, shape and size of the unit cell) and uniform specifications of *k*-mesh, plane-wave basis cutoff energy and size of the simulation cell. Then we analyze the results of our calculations to identify physical trends in the formation and binding energies of the solutes. We would like to note here that although the alkali metals and noble gas atoms do not generally alloy with iron, knowledge of their energetics in iron matrix will be useful to see trends in the solution behavior of atoms in iron. Further, nuclear fission products (including those from molten salt reactors) include elements from alkaline earth, alkali, halogen and noble gas elements. For modeling interaction of these fission products with steel cladding as well as for modeling nuclide distribution between steelmaking phases upon melting of sealed radioactive sources hidden in scrap, knowledge of their solute formation energies are useful [26,27]. Furthermore, oxygen and yttrium atoms are practically immiscible in Fe but ODS steels are produced through mechanical alloying. Similarly, ion-beam mixing is used to mix immiscible Ag, In, and Na in Fe [28,29]. Ion implantation is also used for similar purposes [30,31]. For modeling of such alloying approaches, energetics of these solutes will be useful.

We note further that interactions of self-interstitial atom defects with vacancies and solute elements are also important for a robust understanding of atomic transport in steels [16]. In this work, we do not, however, consider self-interstitial atom defects. The paper is organized as follows. After the introduction in Sec. I, the computational scheme is outlined briefly in Sec. II. In the Results, Sec. III, we show that the solute formation energies, solute size factors, solute-solute and vacancy-solute binding energies vary with the atomic number of the solute atoms in an orderly manner revealing several fundamental trends. Summary of results is given in Sec. IV.

II. COMPUTATIONAL METHOD

We have considered all elements with $Z = 1$ to 54 as solute atoms in bcc Fe. H, C, N, and O were considered as interstitial solute atoms and other atoms as substitutional solutes. Among the interstitial solute atoms, H has been considered as a tetrahedral interstitial solute while the other atoms as octahedral interstitial solutes in accordance with their site preference [32–37]. In order to create point defects in bcc iron, we have used the supercell method. Point defects were introduced into the supercell by adding and/or removing appropriate atoms. An isolated vacancy was created by removing a Fe atom at a given lattice site. Substitutional atom defects were created by replacing a single Fe atom with a solute atom. Substitutional solute-solute pair defects were formed by replacing a pair of nearest-neighbor Fe atoms with a pair of solute atoms. Substitutional vacancy-solute pairs were created by removing a Fe atom at a given site and replacing a Fe atom with a solute atom at a nearest-neighbor (1nn) or a next-nearest-neighbor (2nn) site. Interstitial solute-solute pairs were formed by placing them at nearest-neighbor or further neighbor interstitial sites. This is illustrated in Fig. 1. Vacancy-interstitial atom pairs were formed by removing a Fe atom at a given site and placing the solute at a nearest or next-nearest octahedral interstitial site. A similar procedure is followed for tetrahedral interstitial solute H.

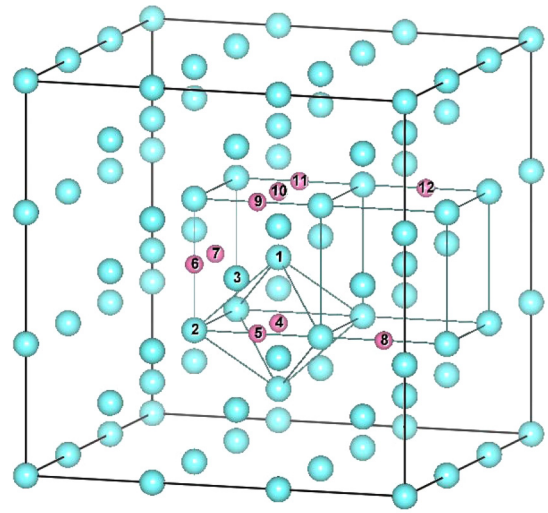

FIG. 1. BCC $3 \times 3 \times 3$ supercell with labeled atoms to define atomic defect configurations. Labels 1, 2, and 3 represent substitutional sites. Labels 4 to 12 represent octahedral interstitial sites. Solute-solute nearest-neighbor pair configuration was obtained by substituting the Fe atoms at sites 1 and 2 with the given solute atoms. Vacancy-solute first and second nearest-neighbor pairs were formed by placing the given solute atom at site 2 or 3, respectively, while site 1 is made vacant. A single interstitial atom defect was formed by placing the atom at site 4. Configurations of pairs of interstitial atoms were created by placing them at pairs of sites 5-6, 5-7, 5-8, 5-9, 5-10, 5-11, and 5-12, respectively, in accordance with Domain *et al.* [34]. Vacancy-interstitial pairs were formed by removing the atom at site 1 and placing an interstitial atom at site 4 or 5, respectively, for 1nn and 2nn configurations [34]. Tetrahedral interstitial sites are not indicated.

Our calculations involve two important energetic quantities, formation and binding energies. The formation energy of a defect is a measure of the amount of energy needed to form the defect. The binding energies are a measure of strength of attractive or repulsive interaction. The vacancy

and solute formation energies and solute-solute and vacancy-solute binding energies were computed from the following expressions [18,21,38]. The formation energy for a vacancy, $E_f^{\square}$, (where $\square$ denotes a vacancy) in bcc iron is calculated from

$$E_f^{\square} = E(\mathrm{Fe}_{N-1}\square_1) - \frac{N-1}{N}E(\mathrm{Fe}_N), \tag{1}$$

where $E(\mathrm{Fe}_{N-1}\square_1)$ is the total energy of an iron supercell with N lattice sites containing a single vacancy and $(N-1)$ Fe atoms. $E(\mathrm{Fe}_N)$ is the total energy of bcc iron supercell with N lattice sites without vacancy defect.

The expression for the formation energy of a substitutional solute, E_f^X, (where a solute atom is denoted by X) is given by [38]

$$E_f^X = E(\mathrm{Fe}_{N-1}X_1) - \frac{\left[N - \left(1+\frac{m}{n}\right)\right]}{N}E(\mathrm{Fe}_N) - \frac{1}{n}E(\mathrm{Fe}_m X_n), \tag{2}$$

where $E(\mathrm{Fe}_{N-1}X_1)$ is the total energy of the iron supercell with N lattice sites containing a solute X and $(N-1)$ Fe atoms. $\mathrm{Fe}_m X_n$ is the reference phase in our calculation of solute formation energy. It is the second phase with which the solid solution phase is in equilibrium (with a common boundary in the phase diagram). It can be a compound phase, elemental crystal, molecules or atoms. Information regarding the second phases in the Fe-X binary systems were obtained from ASM alloy phase diagrams database [39–41]. $E(\mathrm{Fe}_m X_n)$ is the total energy of $\mathrm{Fe}_m X_n$. For an interstitial solute (denoted again by X), the expression for E_f^X is the same except that $(N-1)$ and $(1+\frac{m}{n})$ are replaced by N and $(\frac{m}{n})$, respectively.

The binding energy of a substitutional solute-solute (X-X) pair configuration is given by

$$E_b^{X\text{-}X} = [E(\mathrm{Fe}_{N-2}X_2) + E(\mathrm{Fe}_N)] - 2[E(\mathrm{Fe}_{N-1}X_1)], \tag{3}$$

where $E(\mathrm{Fe}_{N-2}X_2)$ is the total energy of the iron supercell with N sites containing a pair of substitutional solutes X and $(N-2)$ Fe atoms. The expression for the binding energy of a pair of interstitial solutes is given by

$$E_b^{X\text{-}X} = [E(\mathrm{Fe}_N X_2) + E(\mathrm{Fe}_N)] - 2[E(\mathrm{Fe}_N X_1)], \tag{4}$$

where $E(\mathrm{Fe}_N X_2)$ is the total energy of the iron supercell with N lattice sites containing a pair of solutes at interstitial sites and N Fe atoms. $E(\mathrm{Fe}_N X_1)$ is the total energy of the iron supercell of N lattice sites containing N Fe atoms and a solute X at an interstitial site.

For the vacancy-solute ($\square$-X) interaction, the binding energy of a substitutional solute configuration is given by

$$E_b^{\square\text{-}X} = [E(\mathrm{Fe}_{N-2}X_1\square_1) + E(\mathrm{Fe}_N)] - [E(\mathrm{Fe}_{N-1}X_1) + E(\mathrm{Fe}_{N-1}\square_1)], \tag{5}$$

where $E(\mathrm{Fe}_{N-2}X_1\square_1)$ is the total energy of the iron supercell of N lattice sites containing a substitutional solute X, a vacancy ($\square$) and $(N-2)$ Fe atoms. For an interstitial solute, the vacancy-solute binding energy is given by

$$E_b^{\square\text{-}X} = [E(\mathrm{Fe}_{N-1}X_1\square_1) + E(\mathrm{Fe}_N)] - [E(\mathrm{Fe}_N X_1) + E(\mathrm{Fe}_{N-1}\square_1)], \tag{6}$$

where $E(\mathrm{Fe}_{N-1}X_1\square_1)$ is the total energy of the iron supercell of N lattice sites containing a vacancy at a substitutional site, a solute at an interstitial site and $(N-1)$ Fe atoms. With these definitions, negative values of E_b denote binding configurations.

In addition to chemical interactions, the size of the solute atoms also influences the interaction energies of the atomic defects. Therefore, the size factor of solute, SF(X), in bcc iron has been computed using the definition from Hepburn *et al.* [10],

$$SF(X) = \frac{\Delta V}{V_{\mathrm{ave}}} = \frac{V_X - V_{\mathrm{ave}}}{V_{\mathrm{ave}}}, \tag{7}$$

where $V_{\mathrm{ave}} = \frac{V(\mathrm{Fe}_{N-1}X_1)}{N}$ and $V_X = V(\mathrm{Fe}_{N-1}X_1) - \frac{N-1}{N}V(\mathrm{Fe}_N)$. $V(\mathrm{Fe}_{N-1}X_1)$ and $V(\mathrm{Fe}_N)$ are calculated equilibrium volumes of $\mathrm{Fe}_{N-1}X_1$ and Fe_N supercell systems, respectively. Size factors of interstitial solutes are defined in a similar manner.

The total energies required in the calculations of formation and binding energies defined above were computed using $3\times3\times3$ bcc supercells of 54 lattice sites. Previous DFT works on this topic indicate that a $3\times3\times3$ supercell is generally adequate [18,24,32,37,42,43]. The DFT total energy calculations have been performed using the Vienna *ab initio* simulation package (VASP) [44,45]. Projector augmented wave (PAW) potentials [46,47] were used for all the elements considered in this work. For the exchange-correlation functional, the generalized gradient approximation by Perdew, Burke, and Ernzerhof (PBE) [48] was used. All the total energy calculations were fully relaxed with respect to volume as well as all cell-internal and cell-external degrees of freedom, converged to 10^{-8} eV. Methfessel-Paxton order 1 smearing [49] of the Fermi surface was used with a smearing width of $\sigma = 0.2$ eV. It is known that the spin-unpolarized (nonmagnetic) state of bcc Fe is higher in energy than the magnetic state and spin-polarized calculations are necessary to establish its ferromagnetic ground state [24]. The energy difference between the spin-unpolarized and spin-polarized state of Fe can influence the formation and binding energies of solute atoms. Therefore spin-polarized calculations have been performed for all supercells representing pure bcc ferromagnetic iron and bcc iron matrix with vacancy, solute, solute-solute, and vacancy-solute defects. A cutoff energy of 500 eV was used for the plane-wave expansion of the electron wave functions. Extensive tests of k-point sampling have indicated that an extremely dense grid of k points is required for converged atomic defect calculations. Therefore an $8\times8\times8$ k-point mesh generated using the Monkhorst-Pack scheme was used to sample the Brillouin zone. In addition to the total energy of the system, spin-polarized calculations provide the local magnetic moments of the atoms, which can be used to establish the accuracy of our calculations.

With these specifications, the lattice parameter and magnetic moment of bcc Fe were predicted to be 2.84 Å and 2.23 μ_B/atom, respectively. These values are in good agreement with the experimental values of 2.86 Å and 2.2 μ_B/atom [50]. Further, the vacancy formation energy $E_f^{\square} = 2.18$ eV obtained from our calculation is in good agreement with the previously published theoretical values of 2.18 eV [51]

and 2.17 eV [32] as well as with the positron annihilation experimental value of 2.0 ± 0.2 eV [52].

As defined in Eq. (2), computation of the solute formation energies (also known as heat or enthalpy of solution) requires total energies of the pure solute elements or the second phases which exist in equilibrium with the solid solution phase besides the total energies of Fe supercells without/with the solute atoms. Therefore a set of high-precision calculations were performed to determine the total energies of all the pertinent elements and compounds in their respective ground-state structures [39–41]. Spin-polarized calculations have been performed for the elements and compounds according to their respective magnetic order. Appendix gives further details of the calculation of the total energies of all the elements and compounds that were used as reference states.

III. RESULTS AND DISCUSSION

A. Solute formation energies, size factors, and magnetic moments

In Table I, we have collected all the results of our computations of solute formation energy (E_f^X), and solute-solute and vacancy-solute binding energies ($E_b^{X\text{-}X}$ and $E_b^{\square\text{-}X}$) in bcc iron for solutes with atomic numbers 1 to 54 along with their size factors [SF(X)] and magnetic moments (μ_B). For comparison, Table I includes also results from literature, within parentheses, wherever available. We first examine the solute formation energies, E_f^X. Solute formation energies are useful to understand solid state solubility and alloying behavior.

We would like to emphasize a point here: it is a common practice in DFT calculations of formation energy of solute atoms in iron to choose the perfect crystal of the solute element as the reference system [10,18,20,43]. However, this choice is pertinent only if the pure solute element is actually the second phase existing in equilibrium with the solid solution phase. This is indeed true for systems such as Fe-Li, Fe-Na, Fe-Mg, Fe-K, Fe-Ca, Fe-Mn, Fe-Cu, Fe-Rb, Fe-Sr, Fe-Ru, Fe-Ag, Fe-Cd, and Fe-In [39]. But for systems such as Fe-Be, Fe-B, Fe-C, Fe-N, Fe-O, Fe-Al, Fe-Si, Fe-P, Fe-S, Fe-Sc, Fe-Ti, Fe-V, Fe-Cr, Fe-Co, Fe-Ni, Fe-Zn, Fe-Ga, Fe-Ge, Fe-As, Fe-Se, Fe-Y, Fe-Zr, Fe-Nb, Fe-Mo, Fe-Tc, Fe-Rh, Fe-Pd, Fe-Sn, Fe-Sb, Fe-Te, and Fe-I, second phases, other than the solute elements, exist [39]. For these systems, solute formation energies obtained using pure crystals as a reference system can give unphysical equilibrium solubility [38]. For instance, the solute formation energies of Ti, V, Zr, Nb, Al, Si, P, Ga, Ge, and As from Olsson *et al.* [18], You *et al.* [20] and Murali *et al.* [43] give unphysically huge equilibrium concentration of these solutes (regarding the estimation of the equilibrium concentration of solutes, Eq. (6) and the discussion following it in Murali *et al.* [43] could be referred). Therefore, in our work, we have obtained the formation energies of solute atoms with respect to the second phases wherever they are pertinent. Details of the calculation for the reference systems are given in the appendix.

We have compared our formation energies of solutes with literature where the reference state used is the same as in our work. The literature data are often from computational methods. Experimental data of energetics of atomic defects in iron are generally scarce and a comparison of our results with experiments is made wherever possible. We see from column 1 in Table I that our solute formation energy of H (0.194 eV) is in good agreement with a prior DFT result of 0.21 eV [32] and the experimental result of 0.30 eV [64]. For He atoms, the agreement between our work and literature (4.35 versus 4.19 [55] and 4.30 eV [57]) is again very good. For solutes O, Ne, Ar, Cr, Mn, Cu, Ru, Ag, Cd, and In also, our formation energies are in good agreement with literature (within 15%). Only for Xe, our formation energy deviates appreciably from literature. The difference is likely due to the approximate Lennard-Jones empirical potential used in the literature. Although formation energies of other solutes are reported in the literature, they generally correspond to elemental crystal reference states rather than the second phases. Therefore they are not compared with our solution energies.

In order to see whether our solute formation energies predict reasonable solid state solubility, we have computed the equilibrium concentration of the solute atoms C_{eq} by using their formation energies (E_f^X) in the ideal solution expression for solubility $C_{\text{eq}} = \exp(-E_f^X/k_BT)$ [38,43]. Here, k_B is the Boltzmann constant and T is temperature, set to 800 K. The results are listed in Table II. Table II lists also the solubility read from phase diagrams [39]. It should be noted that accurate solubility can be expected if E_f^X in the above expression is replaced by respective free formation energies. Calculating the entropic contributions of electrons, phonons, magnons, and configurational degrees of freedom of the solid solution and the second phases to obtain the free formation energy for all the 53 Fe-X binary systems is beyond the scope of this work. In Table II, solubility is left blank for systems for which phase diagrams are not available.

The important result from our calculation of solute formation energies computed with reference to the corresponding second phases, rather than with respect to pure crystals of solute elements, is that the unphysically huge solubility predicted for certain solutes is now avoided/corrected (Ti, V, Zr, Nb, Al, Si, P, Ga, Ge, As). We see further from Table II that, except for V, As, and Tc, the solubility predicted by our solute formation energies are generally an underestimation compared to those from phase diagrams. This is reasonable because our solubility formula assumes the infinite dilution limit (small solubility limit and negligible interaction between the solute atoms) and ignores entropic contributions to solution free formation energy [38,43]. The overestimation of solubility of V and Tc can be related to the fact that the corresponding second phases (FeV and FeTc) are the Frank-Kasper σ phases which are difficult to model. We have used one of the likely site occupancies reported for the σ-FeCr phase [65] to model FeV and FeTc phases. The reason for overestimation of As solubility is not clear. We have performed total energy calculations for Fe_2As in its antiferromagnetic structure in accordance with literature [66]. Our calculated lattice parameters of Fe_2As match with experimental values.

Figure 2 displays the formation energies of solute atoms (E_f^X) in bcc Fe. We see that the formation energies of solute elements from fourth and fifth periods vary with their atomic numbers such that they reach maxima near the ends of the periods and minima in between, with a local hump near Cu and Ag (like a quasiparabolic valley). Solutes from second

TABLE I. Formation and binding energies of vacancy (□) and solute atoms (X) in bcc iron. All the energies are in eV. Size factor of the solute atoms [SF(X)] and magnetic moments (μ_B) are also listed. For comparison, results from the literature are given within parentheses wherever available.

X	E_f^X	SF(X)	μ_B	$E_b^{X\text{-}X}$	$E_b^{\square\text{-}X}(1nn)$	$E_b^{\square\text{-}X}(2nn)$
H	0.194(0.21) [32]	−0.650	−0.023(−0.05) [53]	−0.026(−0.03) [54]	−0.565(−0.57) [32]	−0.094
He	4.350(4.19) [55]	0.104	0.010(0.05) [55]	−1.140(−0.37) [56]	−0.784(−0.80) [57]	−0.573(−0.50) [57]
Li	0.982	0.075	−0.078	−0.208	−0.235	−0.032
Be	0.395	−0.144	−0.138	−0.085	−0.134	−0.158
B	1.694	−0.31	−0.140	−0.127(−0.05) [35]	−0.236(−0.20) [35]	−0.382(−0.39) [35]
C	0.471	−0.063	−0.146(−0.24) [58]	0.672(0.94) [34]	−0.521(−0.41) [36]	−0.052(0.16) [36]
N	0.210	−0.022	−0.111(−0.14) [58]	0.882(1.19) [34]	−0.786(−0.74) [36]	−0.244(−0.17) [36]
O	1.236(1.24) [43]	0.176	0.044	0.272(0.40) [59]	−1.535(−1.41) [36]	−0.945(−1.02) [36]
F	0.750	0.377	0.170	−0.821	−1.110	−1.240
Ne	5.706(5.76) [56]	0.620	0.018	−1.464(−0.75) [56]	−1.118(−5.41) [56]	−0.396
Na	3.435	0.630	−0.040	−0.60	−0.672	−0.013
Mg	0.971	0.466	−0.053	−0.142	−0.445	0.068
Al	−0.100	0.205	−0.077	0.087(0.09) [20]	−0.307(−0.31) [20]	0.017(0.02) [20]
Si	−0.160	−0.021	−0.089	0.290(0.24) [20]	−0.292(−0.29) [20]	−0.118(−0.11) [20]
P	0.460	−0.095	−0.054	0.209(0.21) [20]	−0.367(−0.37) [20]	−0.256(−0.25) [20]
S	0.760	0.068	0.020	−0.490(−0.51) [20]	−0.535(−0.53) [20]	−0.359(−0.34) [20]
Cl	2.546	0.603	0.138	−1.124	−1.184	−0.600
Ar	7.819(8.03) [56]	1.047	0.175	−1.287(−1.25) [56]	−1.688(−5.83) [56]	−0.745
K	6.963	1.427	0.059	−1.484	−1.819	−0.843
Ca	3.251	1.008	−0.116	−0.510	−1.276	−0.310
Sc	1.122	0.591	−0.407(−0.25) [19]	0.159(0.35) [60]	−0.641(−0.41) [19]	0.171(0.10) [19]
Ti	0.054	0.323(0.32) [18]	−0.797(−0.65) [18]	0.237(0.24) [18]	−0.236(−0.23) [18]	0.188(0.18) [18]
V	−0.286	0.223(0.15) [18]	−1.273(−1.21) [18]	0.227(0.23) [18]	−0.052(−0.05) [18]	0.102(0.09) [18]
Cr	−0.162(−0.14) [18]	0.219(0.15) [18]	−1.803(−0.16) [18]	0.256(0.24) [18]	−0.043(−0.06) [18]	0.001(−0.01) [18]
Mn	0.182(0.21) [18]	0.234(0.02) [18]	−2.015(−0.40) [18]	0.035(−0.06) [18]	−0.192(−0.19) [18]	−0.096(−0.14) [18]
Co	−0.033	0.102(0.03) [18]	1.699(1.72) [18]	0.045(0.04) [18]	0.031(0.03) [18]	−0.101(−0.11) [18]
Ni	0.176	0.266(0.15) [18]	0.890(0.88) [18]	−0.001(−0.02) [18]	−0.086(−0.12) [18]	−0.204(−0.21) [18]
Cu	0.722(0.72) [18]	0.211(0.15) [18]	0.116(0.11) [18]	−0.224(−0.25) [18]	−0.237(−0.27) [18]	−0.181(−0.16) [18]
Zn	0.353	0.319	−0.085	−0.148(−0.14) [60]	−0.320(−0.33) [61]	−0.091
Ga	0.138	0.331	−0.182	0.065(0.12) [20]	−0.382(−0.39) [20]	−0.080(−0.06) [20]
Ge	−0.086	0.301	−0.121	0.270(0.28) [20]	−0.435(−0.44) [20]	−0.128(−0.15) [20]
As	−0.271	0.286	−0.070(−0.05) [62]	0.283(0.29) [20]	−0.510(−0.52) [20]	−0.202(−0.22) [20]
Se	0.930	0.397	−0.019	−0.121(−0.11) [20]	−0.636(−0.62) [20]	−0.281(−0.30) [20]
Br	2.738	0.719	0.064	−0.717	−0.914	−0.379
Kr	8.158	1.165	0.194	−1.156	−1.562	−0.554
Rb	7.928	1.623	0.050	−1.305	−1.947	−0.818
Sr	4.884	1.473	−0.075	−0.743	−1.839	−0.772
Y	2.171	1.196	−0.302(−0.20) [19]	−0.097(0.20) [59]	−1.325(−0.78) [19]	−0.225(−0.02) [19]
Zr	1.128	0.889(1.05) [18]	−0.715(−0.53) [18]	0.226(0.32) [18]	−0.699(−0.67) [18]	0.121(0.06) [18]
Nb	0.231	0.679(0.79) [18]	−0.775(−0.70) [18]	0.299(0.38) [18]	−0.331(−0.32) [18]	0.192(0.13) [18]
Mo	0.036	0.521(0.52) [18]	−0.804(−0.75) [18]	0.256(0.28) [18]	−0.144(−0.13) [18]	0.153(0.10) [18]
Tc	0.084	0.436(0.48) [18]	−0.558(−0.52) [18]	0.056(0.08) [18]	−0.100(−0.11) [18]	0.080(0.02) [18]
Ru	0.293(0.32) [18]	0.426(0.40) [18]	0.326(0.33) [18]	0.070(0.08) [18]	−0.077(−0.09) [18]	0.018(−0.02) [18]
Rh	0.062	0.542(0.58) [18]	0.690(0.70) [18]	0.124(0.16) [18]	−0.114(−0.12) [18]	−0.070(−0.07) [18]
Pd	0.483	0.732(0.81) [18]	0.470(0.40) [18]	−0.015(0.02) [18]	−0.232(−0.25) [18]	−0.160(−0.16) [18]
Ag	1.802(1.93) [18]	0.906(0.92) [18]	0.106(0.01) [18]	−0.403(−0.33) [18]	−0.448(−0.47) [18]	−0.201(−0.20) [18]
Cd	1.768(1.88) [10]	0.921(0.95) [10]	−0.067(−0.06) [10]	−0.366	−0.600	−0.141
In	1.146(1.24) [20]	0.935	−0.234	−0.110(−0.06) [20]	−0.646(−0.68) [20]	−0.071(−0.10) [20]
Sn	0.620	0.895	−0.201(−0.08) [62]	0.285(0.39) [20]	−0.690(−0.71) [20]	−0.051(−0.09) [20]
Sb	0.261	0.837	−0.092(−0.07) [62]	0.601(0.64) [20]	−0.675(−0.71) [20]	−0.095(−0.10) [20]
Te	0.857	0.833	−0.070	0.577(0.68) [20]	−0.746(−0.76) [20]	−0.138(−0.18) [20]
I	3.002	0.933	−0.029	0.181	−0.865	−0.234
Xe	8.267(15.45) [63]	1.405	0.132	−0.611	−1.240	−0.433

TABLE II. Equilibrium concentration of solutes (C_{eq}) in bcc iron obtained from our formation energies listed in Table I compared with the corresponding concentrations from the ASM alloy phase diagrams (PD) database [39] [$C_{eq}(PD)$].

X	C_{eq}	$C_{eq}(PD)$	X	C_{eq}	$C_{eq}(PD)$	X	C_{eq}	$C_{eq}(PD)$
H	0.060	0.05	K	0.000	0.00	Sr	0.000	
He	0.000		Ca	0.000	0.00	Y	0.000	0.00
Li	0.000	0.00	Sc	0.000	0.00	Zr	0.000	0.00
Be	0.003	1.00	Ti	0.450	0.70	Nb	0.040	0.00
B	0.000	0.00	V	57.600	25.00	Mo	0.600	1.00
C	0.001	0.00	Cr	11.000	15.00	Tc	0.295	0.00
N	0.050	0.20	Mn	0.080	2.50	Ru	0.014	2.00
O	0.000	0.00	Co	1.610	30.00	Rh	0.410	8.00
F	0.000		Ni	0.080	5.80	Pd	0.001	0.05
Ne	0.000		Cu	0.000	0.00	Ag	0.000	0.00
Na	0.000	0.00	Zn	0.006	5.00	Cd	0.000	0.00
Mg	0.000	0.00	Ga	0.140	15.00	In	0.000	0.00
Al	4.260	20.00	Ge	3.500	20.00	Sn	0.000	2.00
Si	10.100	28.00	As	49.40	5.00	Sb	0.023	2.00
P	0.001	0.05	Se	0.000	0.00	Te	0.000	1.50
S	0.000	0.00	Br	0.000		I	0.000	0.00
Cl	0.000		Kr	0.000		Xe	0.000	
Ar	0.000		Rb	0.000				

and third periods show a similar trend to the elements near the ends of the fourth and fifth periods. The solute formation energies of H and He are the lowest in the respective groups. We see further that the substantially positive formation energies of alkali (Li, Na, K, Rb), noble gas (He, Ne, Ar, Kr, Xe), alkaline earth (Mg, Ca, Sr), and halogen (F, Cl, Br, I) atoms are in accord with their immiscibility in bcc iron [67]. Se, Ag, and Cd too are immiscible in bcc iron [67]. In agreement with

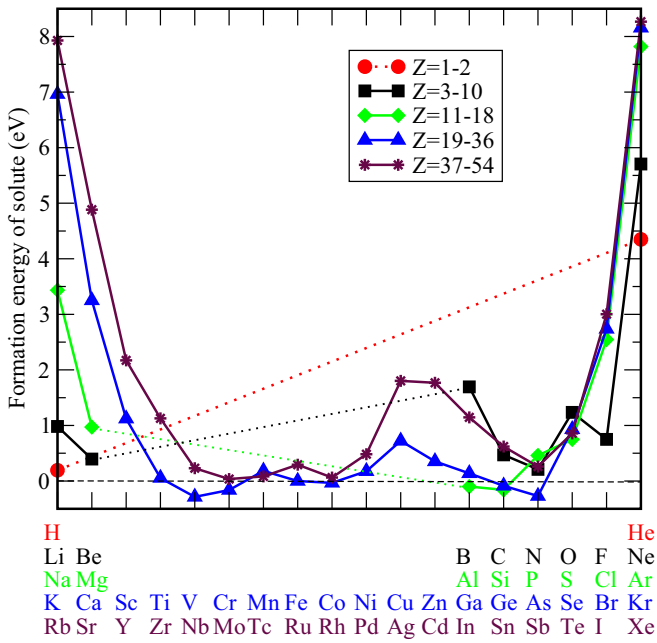

FIG. 2. Formation energies of solute atoms (E_f^X) in bcc Fe. The curves are guides to eye. The dashed horizontal line is a guide to eye delineating negative and positive formation energies.

this, our calculation predicts an appreciably large endothermic formation energies for these solutes. For elements Al, Si, V, Cr, Co, Ge, and As, our calculations predict negative solute formation energies. This is in line with their large solid state solubility in Fe [67]. For other elements H, Be, B, C, N, O, P, S, Sc, Ti, Mn, Ni, Cu, Zn, Ga, Y, Zr, Nb, Mo, Tc, Ru, Rh, Pd, In, Sn, Sb, and Te, our calculations predict moderately positive solute formation energies. Among these, solutes with appreciable solubility such as H, Be, N, P, Ti, Mn, Ni, Zn, Ga, Mo, Ru, Rh, Pd, Sn, Sb, and Te have generally relatively lower formation energies than solutes with negligible solubility such as B, C, O, S, Sc, Cu, Y, Zr, Nb, Tc, and In.

The interaction among atomic defects in a host matrix can have different components. The solute formation energy, presented above, represents the chemical component which is usually the dominant component. The other component that is considered along with the chemical component is the strain component [10,18,23]. The strength of the interaction due to the strain component is to a first approximation proportional to the size factor of the solute atoms in the solvent matrix. Therefore we computed the size factors of the solute atoms [SF(X)] in bcc Fe using Eq. (7), adopted from Hepburn *et al.* [10]. Column 2 of Table I lists these size factors. Comparison of size factors of 3d and 4d transition metal solute atoms from our work with literature [18] is generally satisfactory. For the other 37 solute atoms, size factors are not available in the computational literature and our work provides them for the first time. Measured size factors of substitutional elements are reported [68]. Qualitative agreement is seen between our calculated and the measured size factors, including the negative size factors for Be, P, and Si, despite the significant difference in the solute concentrations involved. (List of measured SF(X) [68]/100: Al(0.128), Be(−0.262), Co(0.015), Cr(0.044), Cu(0.175), Ge(0.165), Mn(0.048), Mo(0.275), Nb(0.176), Ni(0.046), P(−0.132), Pd(0.622), Ru(0.199), Sb(0.364), Si(-0.079), Sn(0.677), Te(0.086), Ti(0.144), V(0.105), and Zn(0.211).)

Figure 3 displays the size factors of the solute atoms. We see that, like formation energies, the size factors of elements from fourth and fifth periods vary with their atomic numbers such that they reach maxima near the ends of the periods and broad minima in between, with a local hump near Ga and In. The size factors of solutes from second and third periods show a similar trend to the solutes near the ends of the fourth and fifth periods. The size factors of H and He are the lowest in their respective groups. The size factor of B deviates from this trend. We performed additional calculations of the solute formation energy and the size factor of B considering it as an octahedral interstitial solute. While the formation energy is found to be almost the same (slightly lower) as that of substitutional B, the size factor is changed significantly (−0.009 for −0.31). With this size factor, the deviation of B is thus corrected. But this change in size factor is not useful to improve the correlations considered in the later sections. Therefore we proceed with substitutional B.

It is further evident that majority of solute atoms have positive size factors. That is, the effective size of these solute atoms in iron matrix is larger than that of iron atoms. This is in agreement with the increase in the lattice parameter of bcc iron with the addition of 3d solute elements [24]. Further, the

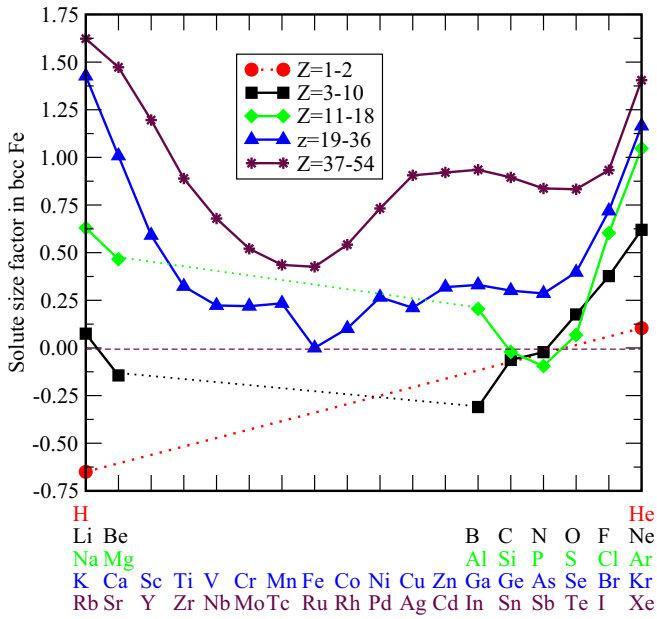

FIG. 3. Size factors of solute atoms [SF(X)] in bcc Fe. The curves are guides to eye.

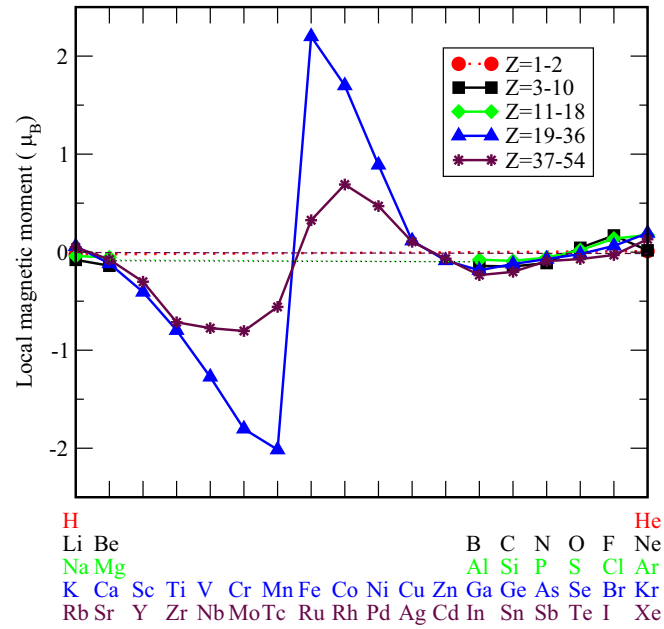

FIG. 4. Local magnetic moments of solute atoms (μ_B) in bcc Fe. The curves are guides to eye.

elements that are identified to be immiscible according to their solute formation energies (He, Li, B, C, O, F, Ne, Na, Mg, S, Cl, Ar, K, Ca, Sc, Cu, Se, Br, Kr, Rb, Sr, Y, Zr, Pd, Ag, Cd, In, Sn, Sb, Te, I, and Xe) also generally have relatively large size factors. He, Li, C, and S are exceptions. These elements are immiscible in iron despite their relatively small size factors. Al, Ti, V, Cr, Mn, Ni, Zn, Ga, Ge, As, Nb, Mo, Ru, and Rh form another set of exceptions. These elements exhibit appreciable solubility though their size factors are relatively large. We will return to the correlation between solute size factor and formation energies in a later section.

Knowledge of magnetic moments of solute elements in iron will be useful for selecting alloying additions with desired magnetic properties. Therefore we have collected the local magnetic moments of all solute atoms considered in this work. Our calculated magnetic moments of solutes (μ_B) are listed in column 4 of Table I. For 3d and 4d transition metal elements as well as for H, He, C, N, Sc, As, Y, Sn, and Sb, our calculated local magnetic moments are found to be in good agreement with literature [10,18,19,53,55,58,62]. For other solute elements our work provides their magnetic moments for the first time. Figure 4 displays the magnetic moments of solutes in bcc iron. We see that the local magnetic moments are not quite significant for solutes from the first, second, and third periods ($Z = 1$ to 18). Solutes from fourth and fifth periods ($Z = 19$ to 36 and $Z = 37$ to 54) have similar magnetic coupling with host Fe. The 3d and 4d transition metal solutes to the left of Fe in the periodic table show antiferromagnetic coupling while those to the right of Fe show ferromagnetic coupling with the host Fe [69]. The magnetic moments of 3d solutes are relatively stronger than those of 4d solutes. Further, it is found that the impurity moments of Ti, V, Cr, Mn, Co, Ni, and Cu obtained from our calculations are in good agreement with neutron scattering experiments and first-principles calculations [69]. Rahman *et al.* have given a mechanism for the antiferromagnetic and ferromagnetic coupling of solute moments with the host moment for 3d transition metal atoms [24]. Through comparison of the spin-unpolarized and polarized impurity-site-projected local density of states (as well as spin density contour plots), they have shown that all 3d electrons from Sc to Cr impurities occupy local minority spin bands (minority spin e_g states) to achieve charge neutrality and consequently to align antiferromagnetically to the host magnetic moments. Additional 3d electrons (from Co, Ni, Cu, Zn impurities) are forced to enter the t_{2g} majority spin states and couple ferromagnetically to the host Fe atoms [24]. While this trend appears to hold for other elements on the left side of the respective periods, it does not hold for solutes on the right side. Rather, solutes from Mg to Ar, Zn to Kr, and Cd to Xe appear to form another group of elements with magnetic coupling similar to 3d or 4d elements with Fe though with weaker moments.

B. Solute-solute binding energy

In an alloy, solute atoms can move randomly in all directions. When they encounter one another, the interaction can be attractive or repulsive, which would cause either precipitation or segregation. Therefore it is useful to obtain the binding energies of pairs of solute atoms in iron. Generally, 1nn solute-solute interactions are dominant compared to further neighbor interactions for substitutional solutes [18,20]. Therefore second and further neighbor solute-solute interaction energies for these solutes have been omitted in our calculations so as to reduce the demanding computational requirements. For interstitial solutes C, N, and O, we have considered their binding energies in seven different configurations. Column 5 of Table I lists nearest-neighbor solute-solute binding energies ($E_b^{X\text{-}X}$) for all the solutes along with results from literature. For 15 solutes, Li, Be, F, Na, Mg, Cl, K, Ca, Br, Kr, Rb, Sr, Cd,

I, and Xe, solute-solute binding energies are not available in the literature and our work provides them for the first time. For the remaining 38 solute atoms, solute-solute binding energies are available in the literature. For 18 of these 38 solutes, our calculated binding energies are in good agreement with literature (within 15%). For the remaining 20 elements (He, B, C, N, O, Ne, Si, Sc, Mn, Ni, Ga, Y, Zr, Nb, Tc, Rh, Pd, Ag, In, and Sn), the difference is more than 15%. Out of these 20 solutes, the literature for He-He and Sc-Sc pairs correspond to different configurations compared to our work. Our work considers a pair of substitutional He atoms whereas literature corresponds to a pair of interstitial He atoms [56]. Similarly, our Sc-Sc pair corresponds to substitutional Sc atoms in a bcc iron matrix modeled with a $3 \times 3 \times 3$ supercell while literature corresponds to a pair of Sc atoms in a fixed free 22-atoms cluster based on bcc structure [60] studied using the Korringa-Kohn-Rostoker Green function method.

Next, we analyze the source of the discrepancy for the remaining 18 systems (B, C, N, O, Ne, Si, Mn, Ni, Ga, Y, Zr, Nb, Tc, Rh, Pd, Ag, In, and Sn). For these systems, as well as for systems where the comparison is satisfactory, the difference between our work and literature is that we have performed the calculations using a 54-atom supercell with zero-pressure conditions using finer k mesh ($8 \times 8 \times 8$) and higher plane-wave energy cutoff (500 eV) but in the literature the calculations have been generally done using a 128-atom supercell with constant-volume condition using coarse k mesh ($3 \times 3 \times 3$) and lower plane wave energy cutoff (300 to 350 eV) [18,20,34,35,56,59]. In order to verify whether the discrepancy in the binding energies is due to the size of the supercell, we have performed additional calculations for the oversized alkali and noble gas atoms (Li, Na, K, Rb, He, Ne, Ar, Kr, and Xe) as their elastic strain fields are expected to extend beyond the $3 \times 3 \times 3$ supercell. Y, Zr, Pd, and B are also included in this calculation of the supercell size convergence test. Table III lists these binding energies.

TABLE III. Solute-solute binding energies ($E_b^{X\text{-}X}$) of selected solute pairs for four different supercell sizes (54, 128, 250, 343 atoms). Calculations with 128- 250- and 343-atom supercells were performed with $6 \times 6 \times 6$, $3 \times 3 \times 3$, and $1 \times 1 \times 1$ k-points meshes respectively.

X-X	54	128	250	343
Li-Li	−0.208	−0.193	−0.197	−0.228
Na-Na	−0.681	−0.650	−0.628	−0.678
K-K	−1.486	−1.333	−1.280	−1.220
Rb-Rb	−1.309	−1.056	−1.020	−1.026
He-He	−1.183	−1.172	−1.174	−1.138
Ne-Ne	−1.463	−1.500	−1.485	−1.477
Ar-Ar	−1.285	−1.216	−1.161	−1.158
Kr-Kr	−1.155	−1.000	−0.895	−0.858
Xe-Xe	−0.611	−0.365	−0.355	−0.341
Y-Y	−0.097	−0.101	−0.045	
Zr-Zr	0.226	0.240	0.261	
Pd-Pd	−0.016	0.017	0.032	
B-B	−0.125	−0.109	−0.106	

TABLE IV. Binding energies ($E_b^{X\text{-}X}$), in eV, between pairs of C, N, and O atoms. The calculations were done using a 54-atom supercell. The distances between the two solute atoms, $d(X\text{-}X)$, are in units of the equilibrium lattice parameter (a). Configuration labels such as "5-6" mean that the atoms are placed at sites labeled 5 and 6 in Fig. 1. For the C-C and N-N pairs, our binding energies are compared with Domain *et al.* [34], given in parenthesis. For the O-O pair, the literature value is from Jiang *et al.* [59].

Configuration	C-C	N-N	O-O	d(X-X)
5-6	0.672 (0.94)	0.882(1.19)	0.272(0.4)	$\sqrt{2}/2$
5-7	0.021 (0.42)	0.148(0.55)	−0.292	$\sqrt{3}/2$
5-8	1.616 (2.28)	1.514(3.03)	1.277	1
5-9	−0.206 (0.17)	0.028(0.27)	−0.402	1
5-10	−0.120 (0.14)	−0.029(0.28)	−0.028	$\sqrt{5}/2$
5-11	−0.226 (0.20)	−0.150(0.29)	−0.244	$\sqrt{2}$
5-12	−0.247 (0.09)	−0.294(0.12)	−0.301	$\sqrt{3}$

It is evident that for Li, Na, He, Ne, and Ar pairs, the binding energies from the 54-atom supercell are converged to within about ±0.1 eV with those obtained from the 128-, 250- and 343-atom supercells. But for K, Rb, Kr, and Xe pairs, this table indicates that one should use at least a 128-atom supercell to achieve similar convergence. Nevertheless, the difference in the binding energies between 54- and 343-atom supercell calculations is still less than 0.3 eV. For Y, Zr, Pd, and B pairs also, similar convergence is seen. Further, the order of the alkali-alkali and noble gas-noble gas binding energies remains similar between the results from 54- and 343-atom supercells.

Next, we consider the binding energies of interstitial solutes C, N, and O. Since C, N, and O are important interstitials in steel and since previous calculations of C-C and N-N binding energies have been generally performed at constant-volume and lower plane-wave cutoff energy [34,58], we have calculated these binding energies at zero-pressure condition. We have included all the seven configurations considered previously for these pairs of interstitials [34]. The results are listed in Table IV. We compare our binding energies of C-C, N-N, and O-O pairs with the corresponding binding energies from literature. (The C-C and N-N interaction energies from literature are presented here without minus sign so as to be consistent with the convention used in this work.) For C-C pairs, our calculations predict a repulsive interaction up to third neighbor separation and attractive interaction beyond this separation, unlike Domain *et al.* where the interaction is repulsive even at sixth neighbor separation. It may be noted that Bhadeshia has studied C-C interactions in iron [70]. One of the conclusions of this study is that the formation of stable clusters of carbon atoms in bcc Fe cannot be ruled out when the distance between pairs of carbon atoms is greater than the near neighbor separation. N-N pairs also show attractive interaction from fourth and farther neighbor separations unlike Domain *et al.* where the interaction is predicted to be repulsive up to sixth-neighbor distances. In the case of O-O pair, our binding energy at the nearest-neighbor distance (0.272 eV) and that from literature (0.4 eV) [59] both suggest repulsive interaction. This interaction becomes attractive from

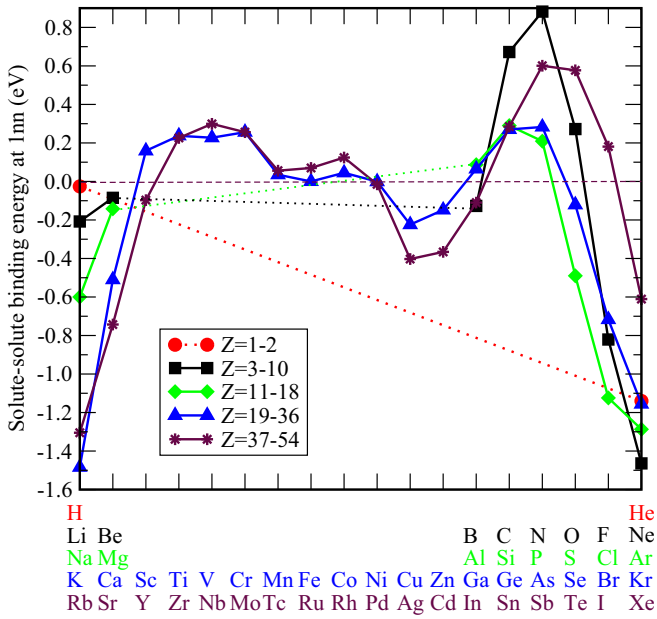

FIG. 5. Solute-solute binding energies ($E_b^{X\text{-}X}$) in bcc Fe at nearest-neighbor positions (1nn). The curves are guides to eye.

second-neighbor distance unlike C-C and N-N pairs where attractive interaction begins at fourth-neighbor distance.

Thus, besides the nature of interactions, we see that the magnitude of our interaction energies also shows some difference with respect to literature. Since the interstitials are additional atoms in the iron matrix, they can be expected to have long-ranged strain fields. Therefore we repeated the C-C and N-N binding energy calculations with $4 \times 4 \times 4$ supercells for configuration "5-12" (see Fig. 1) as it is reported to be stable [34]. These calculations give binding energies of -0.11 and -0.12 eV, respectively. The corresponding binding energies from Domain *et al.* obtained using $4 \times 4 \times 4$ supercell are -0.16 and 0.03 eV, respectively. This shows that the binding energies tend to converge with $4 \times 4 \times 4$ supercell calculations. The remaining difference is likely due to the constant-volume condition and the lower plane-wave cutoff energy ($\leqslant$290 eV) employed in their work.

Figure 5 depicts the solute-solute binding energies listed in column 5 of Table I. We see that the binding energies show a similar but inverse variation with respect to the atomic numbers like the solute formation energies in Fig. 2. That is, strong binding energies occur for solute pairs at the ends of the periods and weak binding energies for pairs from the middle of the periods. Further, the relatively strong binding energies (< -0.2 eV) obtained for the alkali Li, Na, K, Rb, alkaline earth, Ca and Sr, halogen F, Cl and Br, noble gas elements He, Ne, Ar, Kr, Xe, and Cu, Ag, Cd, and S atoms suggest that the driving force for their segregation rather than remaining in solution is quite high, which is in agreement with their immiscibility or limited solubility in bcc iron [67]. Molecular dynamics simulation of He clustering and bubble formation in bcc Fe has shown that isolated He atoms are highly mobile and they aggregate into clusters [71]. Our $E_b^{\text{He-He}}$ indeed suggests clustering of He atoms in Fe.

Our results of solute-solute binding energies further suggest that pairs of 3*d* and 4*d* atoms from Ti to Ni and Zr to Pd show a tendency to repel each other while Cu, Zn, Ag, and Cd have a tendency to cluster, in agreement with previous theoretical studies [5,18]. Among Al, Si, P, and S, S is less soluble in bcc Fe [67]. Accordingly, we obtain an attractive S-S binding energy while repulsive binding energies for Al, Si, and P pairs. You *et al.* have predicted that S, Se, and In with attractive $E_b^{X\text{-}X}$ tend to phase separate. Al, Si, P, Ga, Ge, As, Sn, Sb, Te, with repulsive $E_b^{X\text{-}X}$ tend to be distributed uniformly in the matrix [20]. Our $E_b^{X\text{-}X}$ values confirm both the predictions. We also observe that $E_b^{X\text{-}X}$ are small for H, Be, Al, Mn, Co, Ni, Ga, Y, Tc, Ru, and Pd. Several of these solutes (Al, Co, Ni, Ga) are known to form an extended solid solution in bcc Fe.

C. Vacancy-solute binding energy

As mentioned earlier, the vacancy-solute binding energy is one of the important factors controlling diffusion and solubility of solutes and hence clustering or nucleation of precipitates [17,23,72,73]. In other words, the diffusion coefficients of solute atoms depend on their binding energies with vacancies through migration energies [35,37,74,75]. Vacancy-solute binding energies are also useful for modeling and predicting mechanical behavior of steels under irradiation [76]. Therefore we have computed the binding energies of vacancy-solute ($\square$-X) pairs inserted in a bcc Fe matrix at 1nn and 2nn positions. These energies are listed respectively in columns 6 and 7 in Table I. There are reports of vacancy-solute interaction energies for 38 of the 53 solute atoms considered in this work [18–20,32,35,36,56,57,61]. For the other 15 solutes, i.e., Li, Na, K, Rb, Be, Mg, Ca, Sr, F, Cl, Br, I, Kr, Xe, and Cd, our work provides their binding energies for the first time. For H, Ne, Ar, and Zn, only 1nn pair $E_b^{\square\text{-}X}$ are available from literature. Our work provides both the 1nn and 2nn $E_b^{\square\text{-}X}$.

For C, N, and O, our computed $E_b^{\square\text{-}X}$ are in good agreement with Barouh *et al.* [36] as well as with the experimental binding energy of -0.41 eV for $\square$-C pair [77]. We find further that the binding of these interstitial solutes becomes stronger progressively from C to N to O (-0.521 eV, -0.786 eV, -1.535 eV), which is in agreement with Fu *et al.* [17]. For the other elements also, the comparison of $E_b^{\square\text{-}X}$ between our work and literature is quite satisfactory except for Ne, Ar, Sc, Co, Y, and Pd.

We would like to note that for Al, Si, Ti, V, Cr, Mn, Co, Ni, Cu, Pd, and Sb, $E_b^{\square\text{-}X}$ in bcc Fe are available from muon spin rotation experiments (-0.185 to -0.400, -0.230, -0.160, < -0.105, < -0.105, -0.150, -0.140, -0.215, -0.140, -0.210, and -0.455 eV, respectively [78,79]. A minus sign is included to these binding energies to make them consistent with the convention in our work). For these solutes, the comparison between our binding energies and experiments is very good except for Cu. Our calculation [18,61] overestimates $E_b^{\square\text{-Cu}}$ compared to measurements. We also note that experimental $E_b^{\square\text{-}X}$ is largest for Sb among the solutes listed above. Our computed $E_b^{\square\text{-}X}$ values reproduce this trend exactly. Among Si, P, Cr, Mn, Ni, and Cu, Messina *et al.* have shown that $E_b^{\square\text{-}X}$ is strongest for P and weakest

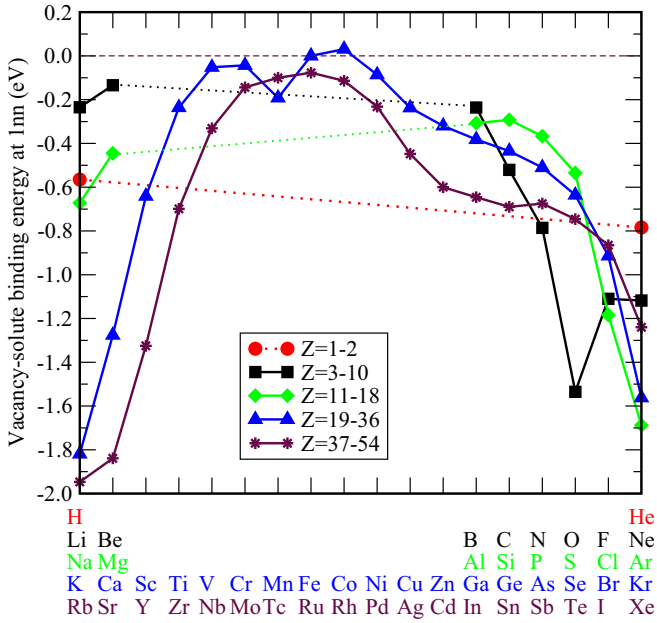

FIG. 6. Vacancy-solute binding energies ($E_b^{\square\text{-}X}$) in bcc Fe at nearest-neighbor positions (1nn).

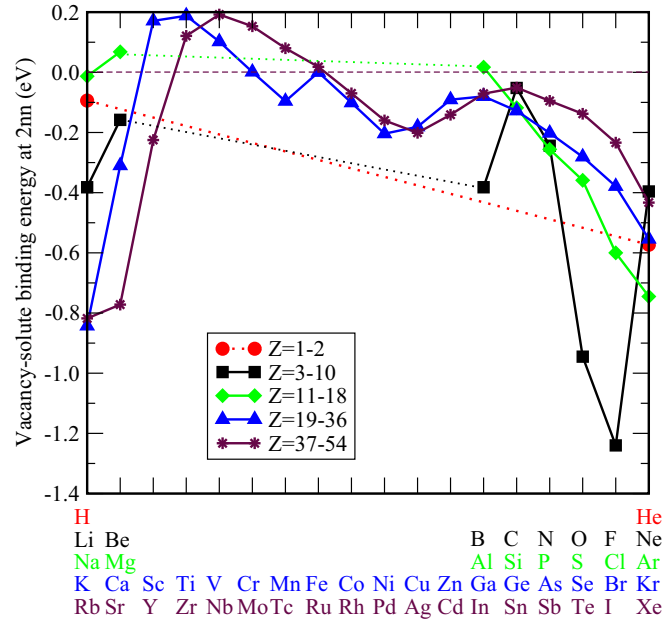

FIG. 7. Vacancy-solute binding energies ($E_b^{\square\text{-}X}$) in bcc Fe at next-nearest-neighbor positions (2nn).

for Cr [72]. Our calculations (Table I) are in accord with this. Further, between Cr and Mo, the $E_b^{\square\text{-}X}$ is predicted to be relatively strong and attractive for Mo in agreement with Olsson *et al.* [18] and Garbatov *et al.* [19]. These results are confirmed by a study of defects in iron-based binary alloys by Mossbauer and positron annihilation spectroscopies [80]. For Co and Ni, $E_b^{\square\text{-}X}$ from literature shows that their 2nn interaction is stronger than 1nn interaction [18,72,73]. Our binding energies reproduce this trend exactly.

Now consider the binding energies of Ne, Ar, Sc, Co, Y, and Pd to vacancy where the comparison is less satisfactory. For Sc and Y, the discrepancy between our binding energy and literature [19] is possibly due to the Green function method with atomic sphere approximation used in their work which precludes relaxation of ionic coordinates. But the trend that $E_b^{\square\text{-}X}$ is stronger for Y than for Sc is retained. For Ne and Ar, we have verified our binding energies with calculations using a 128-atom supercell. Binding energies from these calculations (-1.063 and -1.616 eV, respectively) are found to be in agreement with those obtained using a 54-atom supercell. We think the discrepancy between our work and literature [56] for these solutes is due the lower plane-wave cutoff energy (350 eV) and PW91, rather than PBE, exchange-correlation functional, and the constant volume condition used in their calculations.

Figures 6 and 7 show the binding energies of vacancy-solute pairs at 1nn and 2nn positions in bcc Fe, respectively. We see that, like the solute-solute binding energy in Fig. 5, the binding energies of vacancy-solute pairs show an approximately inverse variation with respect to the atomic numbers of the solutes compared to the solute formation energies in Fig. 2. It is evident that both 1nn and 2nn $E_b^{\square\text{-}X}$ show similar variation with atomic numbers of the solutes. We also note that 1nn binding energies of elements from fifth periods are generally stronger than those of elements from the fourth period, whereas the 2nn binding energies of $3d$ and sp elements from the fourth period are generally stronger than those of the corresponding elements from the fifth period. We further see from Figs. 6 and 7 that the $E_b^{\square\text{-}X}$ at 1nn is attractive (exothermic) for all solutes except Co while the 2nn $E_b^{\square\text{-}X}$ have become repulsive (endothermic) for some solutes (Al, Mg, Sc, Ti, V, Cr, Zr, Nb, Mo, Tc, and Ru). Comparison of Fig. 6 with 5 also shows that $E_b^{\square\text{-}X}$ at 1nn is attractive for all solutes unlike $E_b^{X\text{-}X}$, which are repulsive for many solute pairs.

Figure 7 shows that the 2nn $E_b^{\square\text{-}X}$ is repulsive for early transition metal solutes and attractive for late transition metal solutes in agreement with literature [18]. We see that the strongest vacancy-solute binding occurs for solutes K, Rb, Sr, Ar, Kr, Ca, O, Y, and Xe, and the weakest binding for solutes V, Cr, Co, Ni, and Ru. This suggests that the solutes K, Rb, Sr, Ar, Kr, Ca, O, Y, and Xe, when present in bcc Fe matrix, will trap vacancies strongly. This is known to be true for O and Y [17,81].

Figure 8 is a graph of 1nn $E_b^{\square\text{-}X}$ for $3d$ and $4d$ transition metal atoms from our work plotted with respect to their corresponding calculated diffusion coefficients by Messina *et al.* [73]. It is interesting to note that our $E_b^{\square\text{-}X}$ of $4d$ solutes show an inverse parabolic variation to their calculated tracer diffusion coefficients at 1100 K [73] (see their Fig. 9). For the $3d$ transition metal solutes a similar correlation is evident too. This observation suggests that $E_b^{\square\text{-}X}$ of other solutes predicted in our work would provide a guide to judge their diffusion coefficients.

Gorbatov *et al.* have earlier considered $E_b^{\square\text{-}X}$ and diffusion in iron. They have identified that the attractive 1nn $E_b^{\square\text{-}X}$ of most of the solutes correlate well with the experimental data on impurity diffusion coefficients, which are systematically higher than the Fe self-diffusion coefficient [19]. Our $E_b^{\square\text{-}X}$ for an extended set of solute elements show that the attractive

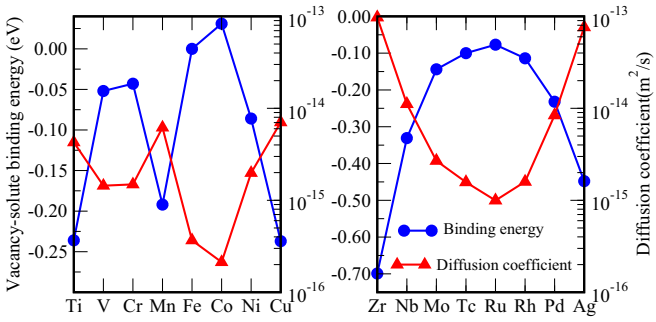

FIG. 8. Vacancy-solute binding energies of 3*d* and 4*d* transition metal atoms in bcc Fe at nearest-neighbor positions from our work plotted against the corresponding calculated diffusion coefficients from Messina *et al.* [73] (their Fig. 9).

1nn vacancy-solute interaction is generally retained. This appears to be in agreement with the observation that in iron even the oversized solute atoms have higher diffusion coefficients than self-diffusion coefficients as well as with the suggested absence of slow diffusers among the common solute additions to bcc Fe [4,81].

D. Discussion

Next, we analyze the formation and binding energies of solutes and their size factors to see if they are correlated. We begin with a discussion of the effect of solute size on its formation energy. Figure 9 shows our calculated formation energies of solute atoms as a function of their size factors in bcc iron [E_f^X versus SF(X)]. The horizontal dotted line at the solute formation energy of 1 eV is a guide to eye separating data points below and above 1 eV. The vertical dotted line at size factor 1 separates data points below and above 1. The solute atoms that form alloys with iron generally have size factors below 1 and formation energies below 1 eV whereas elements that do not normally alloy with iron (Li, Na, K, Rb, He, Ne, Ar, Kr, Xe, F, Cl, Br, I, Mg, Ca, Sr, Ag, Cd, In, and Y) [67] generally have solute formation energies above 1 eV. Many of the later also have size factors above 1. That is, a correlation between solute formation energies and size factors exists for some elements but is absent for other elements. For example, the size factors of solutes He, Li, S, and Co are near 0.1. But their formation energies change from about 4 eV to about −0.03 eV.

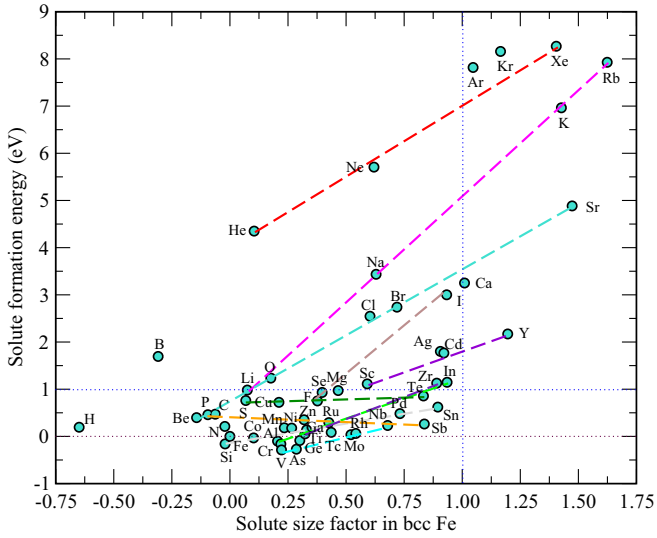

FIG. 9. Formation energy vs size factor of solute atoms [E_f^X vs SF(X)] in bcc Fe. The dashed lines are guides to eye indicating a correlation between the formation energy and the size factor of solute atoms along columns in the periodic table. Note that we have drawn only a few lines to illustrate this correlation though it exists along other groups as well.

Other trends also emerge from Fig. 9. By comparing isoelectronic sets of solutes (i.e., solutes in the same column or group of the periodic table, H/Li/Na/K/Rb, Be/Mg/Ca/Sr, Sc/Y, Ti/Zr, V/Nb, Cr/Mo, Mn/Tc, Fe/Ru, Co/Rh, Ni/Pd, Cu/Ag, Zn/Cd, B/Al/Ga/In, C/Si/Ge/Sn, N/P/As/Sb, O/S/Se/Te, F/Cl/Br/I, and He/Ne/Ar/Kr/Xe), one can see a clear trend that the size factor increases down the groups with an associated increase in the solute formation energy, indicated by dashed lines drawn as a guide to eye. Solutes H, B, C, N, and O are exceptions to this trend. This graph thus shows that the solute size factor and its influence on the solute formation energy are quite appreciable along the groups rather than across the periods. Another physical trend that may be noticed is that the rate of increase of solute formation energy with the size factor is less along V/Nb, Cr/Mo, Mn/Tc, Co/Rh, and Ni/Pd groups compared to alkali, alkaline earth, halogen, and noble gas atoms. The higher rate of increase of solute formation energies with size factors, for instance, for alkali elements or noble gas atoms, is likely because the strain component (size factor) of the interactions is more dominant than the chemical component. This also indicates, for instance, that the solubility of He in iron will increase appreciably with high pressure compared to the solubility of Nb or Mo.

Figure 10 is a graph of vacancy-solute binding versus solute size factor in bcc iron [$E_b^{\square\text{-}X}$ vs SF(X)]. The horizontal dotted line at $E_b^{\square\text{-}X} = -0.8$ eV is a guide to eye separating data points below and above −0.8 eV. It is evident that the common alloying elements in steel have their vacancy-solute binding energies above −0.8 eV and size factors within −0.25 and 1. The relatively weak vacancy-solute binding energies of these solute atoms are likely due to their strong bonding with the Fe atoms. Because of this strong X-Fe bonding, it is unfavorable for a solute atom to be placed near a vacancy, since this will result in fewer X-Fe bonds. The data points with binding energies below about −0.8 eV include solutes O, F, Ne, Cl, Ar, K, Ca, Br, Kr, Rb, Sr, Y, I, and Xe. Several of these solutes also have large size factors.

The strong $E_b^{\square\text{-}X}$ with associated $SF(X)$ seen for some of these solutes (Ar, Kr, Xe, K, Rb, Ca, Sr, and Y), in an overall sense, may be understood by a simple physical argument: placing large impurity atoms in the Fe matrix induces a significant strain on the surrounding Fe atoms. A vacancy next to this large impurity allows the impurity to relax towards the vacancy and hence away from the other neighboring Fe atoms. Thus a vacancy in a 1nn position to a large impurity helps to relieve the strain, producing an energy lowering of

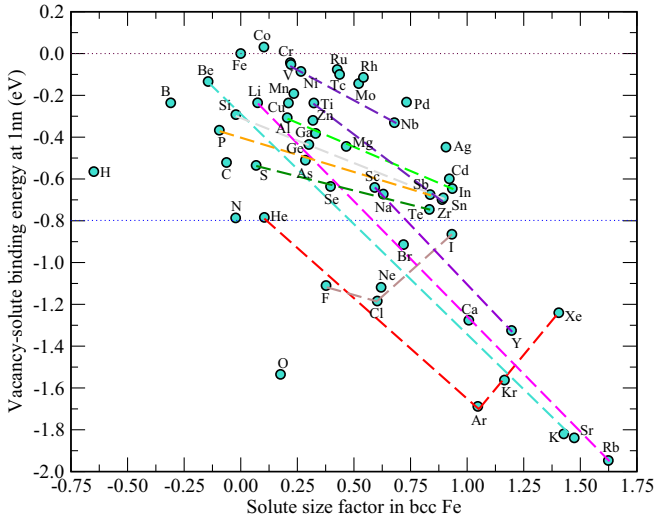

FIG. 10. Vacancy-solute binding energy vs solute size factor [$E_b^{\square\text{-}X}$ vs SF(X)] in bcc Fe. The dashed lines indicate trends along the groups. Similar trends can be seen along the other groups also.

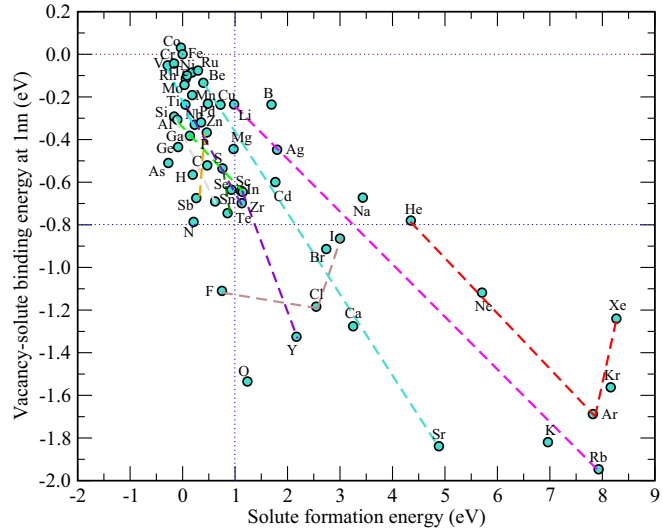

FIG. 11. Vacancy-solute binding energy vs solute formation energy ($E_b^{\square\text{-}X}$ vs E_f^X) in bcc Fe. The dashed lines are drawn to indicate the correlations between $E_b^{\square\text{-}X}$ and E_f^X along the groups.

the $\square$-X pair, and hence a stronger binding energy. However, this mechanism is inadequate to explain the relatively small $E_b^{\square\text{-}X}$ of solutes with relatively large size factors such as Ag, Cd, In, Sn, Zr, and Sb, and the large binding energies of O and F with relatively small size factors.

Figure 10 reveals other correlations as well. Isoelectronic sets of solutes (i.e., H/Li/Na/K/Rb, Be/Mg/Ca/Sr, Sc/Y, Ti/Zr, V/Nb, Cr/Mo, Mn/Tc, Fe/Ru, Co/Rh, Ni/Pd, Cu/Ag, Zn/Cd, B/Al/Ga/In, C/Si/Ge/Sn, N/P/As/Sb, O/S/Se/Te, F/Cl/Br/I, and He/Ne/Ar/Kr/Xe) reveal a clear trend that the strength of vacancy-solute binding energies increases with increasing size factor down the columns, indicated by dashed lines. We see also that the rate of increase of vacancy-solute binding with the size factor is less along V/Nb, Cr/Mo, Co/Rh, and Ni/Pd groups. Solutes H, B, C, N, and O are exceptions. Mn/Tc, and halogen and noble gas atoms (F, Cl, Br, I, He, Ne, Ar, Kr, and Xe) also show deviations from this trend. For halogen and noble gas elements, $E_b^{\square\text{-}X}$ increases initially (from F to Cl, and from He to Ar) with the size factors and then decreases with further increase in the size factors (Cl to I, and Ar to Xe). This may be understood as follows: these atoms behave more like hard spheres in the iron matrix (unlike, for instance, alkali elements with a strong tendency to loose electrons). The size factors of F and Cl as well as He, Ne, and Ar are relatively smaller that they can relieve their stresses by relaxing to the nearby vacancy site. But this is not effective for solutes with size factors beyond certain limit (Br and I as well as Kr and Xe), which manifests in the reduction of $\square$-X binding. The deviation of Mn/Tc is likely due to the complex magnetic property of Mn, which is missing from our DFT calculation. We will consider the vacancy-interstitial solutes interaction later.

Figure 11 is a graph of vacancy-solute binding energy versus solute formation energy ($E_b^{\square\text{-}X}$ versus E_f^X). The vertical and horizontal lines are guides to eye. It is apparent that $E_b^{\square\text{-}X}$ is correlated to E_f^X, similar to $E_b^{\square\text{-}X}$ versus SF(X) (Fig. 10). It is further evident that most of the common alloying elements have their solute formation energies below 1 eV with vacancy-solute binding energies between 0.1 and -0.8 eV. Insoluble solute atoms with large formation energies such as He, Li, Ne, Na, Cl, Ar, K, Ca, Br, Kr, Rb, Sr, Y, Ag, Cd, In, I, and Xe have strong binding energy with vacancy. O and F are also insoluble in iron but their E_f^X are moderate like those of common alloying elements. Nevertheless, their binding energies with vacancy are strong like those of insoluble atoms. H, B, C, N, O, Mn/Tc, halogen, and noble gas atoms are exceptions. We relate the deviations seen with the later elements to the same reasons discussed in the previous paragraph. The recurrent exceptions of interstitial solute atoms with respect to the several groupwise correlations considered above remains to be explained. On the other hand, the experimental solution enthalpy and size factor of C in bcc Fe (solution enthalpy 0.60 to 0.78 eV and 1.10 eV as reported in Refs. [22,37], respectively, and size factor 0.781 as reported in Ref. [82]) lead to further deviation of C from the groupwise correlation (in Fig. 9). Comparison of experimental size factors of C, Si, Ge, and Sn (0.781, -0.078, 0.165, and 0.677) [68,82] also leads to similar conclusion. That is, the deviations of H, B, C, N, and O from the groupwise trends is real. Thus our computed energetics of atomic defects in bcc Fe reveal several fundamental trends and will be useful for identifying solutes or combination of solutes with desired diffusion property that can be used to optimize the coarsening kinetics and creep strength of steels.

IV. SUMMARY AND CONCLUSIONS

In order to understand the atomic level properties of steels, we have performed an extensive set of first-principles electronic structure calculations of the formation and binding energies of atomic defects (vacancy, solute atoms, solute-solute, and vacancy-solute pairs) in ferromagnetic bcc iron. An extended set of solute elements with atomic numbers from 1 to 54 have been considered. Our calculations reveal several

trends in the formation and binding energies of solutes and their size factors. (1) It is found that the formation energies of solutes from fourth and fifth periods vary with their atomic numbers such that they reach maximum near the ends of the periods and minimum in between, with a local hump near Cu and Ag (like a quasiparabolic valley). Solutes from the second and third periods show similar trends like the elements near the ends of the fourth and fifth periods. The common solute additions to Fe ($3d$, $4d$, and sp elements) are found to possess moderate formation energies. Large endothermic formation energies are obtained for solutes that lack solubility in Fe (alkali, halogen, noble gas, alkaline earth, Se, Ag, an Cd atoms). (2) Like formation energies, the size factors of the solute elements also vary with their atomic numbers such that they reach maximum near the ends of the periods and minimum in between. The majority of solute atoms have positive size factors, i.e., their effective sizes in the iron matrix are higher than that of iron atoms. Immiscible solute atoms generally possess relatively large size factors. (3) Solubilities estimated from our formation energies are found to be in reasonable agreement with those from the phase diagram database.

(4) The solute-solute and vacancy-solute binding energies vary with the atomic number of the solutes in a manner inverse to the formation energies and size factors. That is, strong binding energies occur for solute-solute or vacancy-solute pairs at the ends of the periods and weak binding energies for pairs from the middle of the periods. We also find that the 1nn solute-solute binding is repulsive for many solute pairs while vacancy-solute binding is always attractive. (5) The size factors of isoelectronic sets of elements increase down the groups with an associated increase of the formation energies. The strength of the solute-solute and vacancy-solute binding energy increases with the size factors of solutes down the groups. (6) Comparison of our predicted vacancy-solute binding energies of $3d$ and $4d$ transition elements with their corresponding calculated diffusion coefficients from literature shows a significant correlation whereby solutes with strong binding energies possess higher diffusion coefficients and vice versa. This in turn indicates that our predicted vacancy-solute binding energies of other solutes are useful to estimate their diffusion coefficients.

ACKNOWLEDGMENTS

E.A.D. acknowledges HBNI/IGCAR research fellowship support. The first two authors also acknowledge the Computing Systems Section of IGCAR for computer facility and Dr. T. R. Ravindran and Dr. R. Rajaraman for fruitful discussions.

APPENDIX: GROUND-STATE TOTAL ENERGY OF REFERENCE SYSTEMS

For the calculation of solute formation energies in bcc Fe, the total energies of the elemental solutes (X) or Fe-X binary compounds, whichever is in equilibrium with the solid solution phase (Fe), are required. For this, we performed a set of high-precision calculations for the ground-state structure of all the pertinent elements and compounds. The crystal structures of the elements and compounds include body centered cubic (bcc), face centered cubic (fcc), hexagonal close packed (hcp), tetragonal, orthorhombic, and trigonal symmetries with nonmagnetic, ferromagnetic, or antiferromagnetic orders. The ground-state crystallographic parameters were determined through full relaxation of the unit cell and atomic positions. To ensure that the total energies and lattice parameters were determined accurately, we used a plane-wave cutoff energy of 500 eV, a high-density Monkhorst-Pack k-point grid to sample the Brillouin zone, and an energy tolerance of 10^{-8} eV. We tested convergence with respect to k-point mesh for each system beginning with a coarse mesh, and k-point meshes used for all the systems are listed in Table V. With these settings, the lattice parameters of most of the elements and compounds were reproduced within $\pm 2\%$ of experimental lattice parameters, which are also listed in Table V.

For H, F, Cl, and Br, the spin-polarized electronic energy of their free diatomic molecules has been used as their reference state energy. We have performed these free molecular calculations by placing a single diatomic molecule in a 7 Å cubic cell and optimized the bond length. Optimized bond lengths (0.75, 1.42, 1.99, 2.32 Å) were found to be in good agreement with their respective experimental bond lengths (0.74, 1.41, 1.99, 2.27 Å).

For noble gas atoms, the spin-polarized electronic energy of their free atoms has been used as their reference state energy. These free atom calculations were performed by placing a single atom at the center of a 12-Å cubic cell.

Spin-polarized calculations were performed for all the crystalline systems with ferromagnetic or antiferromagnetic order. For FeO, FeS, Fe_2Ti, Fe_2As, Fe_2Nb, FeSn, FeSb, and $Fe_{1.12}Te$, antiferromagnetic calculations have been performed in accordance with their respective literature [66,83–89]. For Cr, a commensurate antiferromagnetic spin structure has been assumed [90]. Specifying the AFM unit cell of FeI_2 in the DFT calculation is not straightforward. Therefore calculations were performed with the $FeCl_2$-type AFM order [91]. For Mn, a nonmagnetic calculation in the bcc structure with 58 atoms (α-Mn) was performed. The total energy of Mn was then corrected by 28 meV, the energy by which its antiferromagnetic state is reported to be more stable than the nonmagnetic state [10].

Further, the second phases are not always line compounds. $FeBe_2$, FeO, Fe_3Al, FeS, Fe_2Ti, FeV, FeCo, Fe_3Zn_{10}, Fe_3Ga, Fe_3Ge, Fe_2Zr, Fe_2Nb, FeTc, FeRh, FePd, FeSb, and $Fe_{1.12}Te$ all exhibit significant homogeneity range. Some of them also have complex magnetic structure and multiple or partial site occupancies. The total energies of these phases were computed for the crystallographic parameters given in the literature [40,41]. Determining the minimum energy composition of these phases over their respective homogeneity range is beyond the scope of this work.

TABLE V. Calculation details for the ground-state total energy of elemental (X) and binary Fe-X phases considered as reference systems for the formation energy of solutes (X) in bcc Fe. Space group, magnetic order, lattice parameters (a, b, c) (Å), k mesh, and valence electron configurations of the solutes (X) in their respective VASP-PAW potentials are listed. Space groups are given along with space group numbers in parentheses. Labels NM, FM, and AFM denote nonmagnetic, ferromagnetic, and antiferromagnetic orders, respectively. Calculated equilibrium lattice parameters are compared with experimental values given in parentheses. Measured crystal structure data of the elements and Fe-X binary compounds were taken from Pearson's handbook of crystallographic data [40] and Pauling file [41]. The size of the simulation box used for free atom and free molecule systems is also denoted by "a."

Phase	Space group	Magnetic order	Lattice parameter	k mesh	Valence shell of X
H	Free molecule	NM	$a = 7$	$1 \times 1 \times 1$	$1s^1$
He	Free atom	NM	$a = 12$	$1 \times 1 \times 1$	$1s^2$
Li	Im-$3m$ (229)	NM	$a = 3.440(3.510)$	$17 \times 17 \times 17$	$2s^1 2p^0$
$FeBe_2$	$P63/mmc$ (194)	FM	$a = 4.175(4.212)$	$7 \times 7 \times 7$	$2s^2 2p^0$
			$c = 6.794(6.853)$		
Fe_2B	$I4/mcm$ (140)	FM	$a = 5.054(5.117)$	$9 \times 9 \times 9$	$2s^2 2p^1$
			$c = 4.236(4.252)$		
Fe_3C	$Pnma$ (62)	FM	$a = 5.021(5.078)$	$11 \times 11 \times 11$	$2s^2 2p^2$
			$b = 6.740(6.733)$		
			$c = 4.480(4.519)$		
Fe_4N	Pm-$3m$ (221)	FM	$a = 3.795(3.795)$	$7 \times 7 \times 7$	$2s^2 2p^3$
FeO	Fm-$3m$ (225)	AFM	$a = 4.312(4.321)$	$17 \times 17 \times 17$	$2s^2 2p^4$
F	Free molecule	NM	$a = 7$	$1 \times 1 \times 1$	$2s^2 2p^5$
Ne	Free atom	NM	$a = 12$	$1 \times 1 \times 1$	$2s^2 2p^6$
Na	Im-$3m$ (229)	NM	$a = 4.200(4.290)$	$17 \times 17 \times 17$	$3s^1 3p^0$
Mg	$P63/mmc$ (194)	NM	$a = 3.200(3.210)$	$17 \times 17 \times 17$	$3s^2 3p^0$
			$c = 5.200(5.210)$		
Fe_3Al	Fm-$3m$ (225)	FM	$a = 5.744(5.800)$	$7 \times 7 \times 7$	$3s^2 3p^1$
FeSi	$P213$ (198)	FM	$a = 4.450(4.484)$	$9 \times 9 \times 9$	$3s^2 3p^2$
Fe_3P	I-4 (82)	FM	$a = 9.051(9.107)$	$4 \times 4 \times 7$	$3s^2 3p^3$
			$c = 4.382(4.460)$		
FeS	$P63/mmc$ (194)	AFM	$a = 3.410(3.448)$	$15 \times 15 \times 15$	$3s^2 3p^4$
			$c = 5.710(5.744)$		
Cl	Free molecule	NM	$a = 7$	$1 \times 1 \times 1$	$3s^2 3p^5$
Ar	Free atom	NM	$a = 12$	$1 \times 1 \times 1$	$3s^2 3p^6$
K	Im-$3m$ (229)	NM	$a = 5.30(5.33)$	$17 \times 17 \times 17$	$3p^6 4s^1$
Ca	Fm-$3m$ (225)	NM	$a = 5.53(5.58)$	$17 \times 17 \times 17$	$3s^2 3p^6 4s^2$
Fe_2Sc	$P63/mmc$ (194)	FM	$a = 4.920(4.937)$	$9 \times 9 \times 7$	$3s^2 3p^6 4s^2 3d^1$
			$c = 8.066(8.038)$		
Fe_2Ti	$P63/mmc$ (194)	AFM	$a = 4.705(4.757)$	$7 \times 7 \times 5$	$3p^6 3d^3 4s^1$
			$c = 7.811(7.829)$		
FeV	$P42/mnm$ (136)	FM	$a = 8.987(8.965)$	$5 \times 5 \times 9$	$3p^6 3d^4 4s^1$
			$c = 4.580(4.633)$		
Cr	Im-$3m$ (229)	AFM	$a = 2.88(2.91)$	$17 \times 17 \times 17$	$3p^6 3d^5 4s^1$
Mn	I-43m (217)	NM	$a = 8.57(8.91)$	$6 \times 6 \times 6$	$3p^6 4s^2 3d^5$
Fe	Im-$3m$ (229)	FM	$a = 2.84(2.86)$	$17 \times 17 \times 17$	$3p^6 4s^1 3d^7$
FeCo	Pm-$3m$ (221)	FM	$a = 2.846(2.856)$	$17 \times 17 \times 17$	$3d^8 4s^1$
FeNi	$P4/mmm$ (123)	FM	$a = 2.520(2.533)$	$17 \times 17 \times 17$	$3d^8 4s^2$
			$c = 3.581(3.582)$		
Cu	Fm-$3m$ (225)	NM	$a = 3.63(3.61)$	$17 \times 17 \times 17$	$3d^{10} 4s^1$
Fe_3Zn_{10}	I-43m (217)	FM	$a = 8.976(8.978)$	$5 \times 5 \times 5$	$3d^{10} 4s^2$
Fe_3Ga	Pm-$3m$ (221)	FM	$a = 3.658(3.679)$	$17 \times 17 \times 17$	$4s^2 4p^1$
Fe_3Ge	$P63/mmc$ (194)	FM	$a = 5.142(5.160)$	$9 \times 9 \times 9$	$4s^2 4p^2$
			$c = 4.224(4.210)$		
Fe_2As	$P4/nmm$ (129)	AFM	$a = 3.635(3.634)$	$6 \times 6 \times 3$	$4s^2 4p^3$
			$c = 5.920(5.985)$		
FeSe	$P4/nmm$ (129)	FM	$a = 3.600(3.710)$	$13 \times 13 \times 9$	$4s^2 4p^4$
			$c = 5.880(6.010)$		
Br	Free molecule	NM	$a = 7$	$1 \times 1 \times 1$	$4s^2 4p^5$
Kr	Free atom	NM	$a = 12$	$1 \times 1 \times 1$	$4s^2 4p^6$
Rb	Im-$3m$ (229)	NM	$a = 5.59(5.67)$	$17 \times 17 \times 17$	$4p^6 5s^1$

TABLE V. *(Continued.)*

Phase	Space group	Magnetic order	Lattice parameter	k mesh	Valence shell of X
Sr	Fm-3m (225)	NM	$a = 6.02(6.08)$	17 × 17 × 17	$4s^2 4p^6 5s^2$
$Fe_{17}Y_2$	$P63/mmc$ (194)	FM	$a = 8.481(8.462)$ $c = 8.257(8.282)$	5 × 5 × 5	$4s^2 4p^6 5s^2 4d^1$
Fe_2Zr	Fd-3m (227)	FM	$a = 7.043(7.017)$	9 × 9 × 9	$5s^2 4d^1 5p^1$
Fe_2Nb	$P63/mmc$ (194)	AFM	$a = 4.774(4.840)$ $c = 7.793(7.895)$	9 × 9 × 9	$4p^6 5s^1 4d^4$
Fe_2Mo	$P63/mmc$ (194)	FM	$a = 4.675(4.745)$ $c = 7.797(7.734)$	9 × 9 × 9	$4p^6 5s^1 4d^5$
FeTc	$P42/mnm$ (136)	FM	$a = 9.105(9.130)$ $c = 4.885(4.788)$	5 × 5 × 9	$4p^6 5s^1 4d^6$
Ru	$P63/mmc$ (194)	NM	$a = 2.73(2.71)$ $c = 4.32(4.28)$	17 × 17 × 17	$4p^6 5s^1 4d^7$
FeRh	Pm-3m (221)	FM	$a = 3.016(2.989)$	17 × 17 × 17	$4p^6 5s^1 4d^8$
FePd	$P4/mmm$ (123)	FM	$a = 2.738(2.722)$ $c = 3.751(3.715)$	17 × 17 × 17	$5s^1 4d^9$
Ag	Fm-3m (225)	NM	$a = 4.160(4.080)$	17 × 17 × 17	$5s^1 4d^{10}$
Cd	$P63/mmc$ (194)	NM	$a = 3.050(2.980)$ $c = 5.700(5.620)$	17 × 17 × 17	$5s^2 4d^{10}$
In	$I4/mmm$ (139)	NM	$a = 3.33(3.25)$ $c = 4.96(4.95)$	17 × 17 × 17	$5s^2 5p^1$
FeSn	$P6/mmm$ (191)	AFM	$a = 5.290(5.297)$ $c = 4.430(4.481)$	7 × 7 × 7	$5s^2 5p^2$
FeSb	$P63/mmc$ (194)	AFM	$a = 3.980(4.060)$ $c = 5.028(5.130)$	15 × 15 × 15	$5s^2 5p^3$
$Fe_{1.12}Te$	$P4/nmm$ (129)	AFM	$a = 3.679(3.812)$ $c = 6.505(6.251)$	5 × 5 × 3	$5s^2 5p^4$
FeI_2	P-3m1 (164)	AFM	$a = 4.015(4.040)$ $c = 7.108(7.375)$	7 × 7 × 5	$5s^2 5p^5$
Xe	Free atom	NM	$a = 12$	1 × 1 × 1	$5s^2 5p^6$

[1] I.-S. Kim, J. D. Hunn, N. Hashimoto, D. L. Larson, P. J. Maziasz, K. Miyahara, and E. H. Lee, J. Nucl. Mater. **280**, 264 (2000).

[2] R. L. Klueh, J. P. Shingledecker, R. W. Swindeman, and D. T. Hoelzer, J. Nucl. Mater. **341**, 103 (2005).

[3] T. Schuler, M. Nastar, and F. Soisson, Phys. Rev. B **95**, 014113 (2017).

[4] S. Huang, D. L. Worthington, M. Asta, V. Ozolins, G. Ghosh, and P. K. Liaw, Acta Mater. **58**, 1982 (2010).

[5] O. I. Gorbatov, A. H. Delander, Y. N. Gornostyrev, A. V. Ruban, and P. A. Korzhavyi, J. Nucl. Mater. **475**, 140 (2016).

[6] A. Somoza and A. Dupasquier in *Fundamentals of Aluminium Metallurgy Production, Processing and Applications*, edited by R. Lumley (Woodhead Publishing Limited, Cambridge, UK, 2011), p. 386.

[7] M. W. Zandbergen, Q. Xu, A. Cerezo, and G. D. W. Smith, Acta Mater. **101**, 136 (2015).

[8] W. W. Xu, S. L. Shang, B. C. Zhou, Y. Wang, L. J. Chen, C. P. Wang, X. J. Liu, and Z. K. Liu, Phys. Chem. Chem. Phys. **18**, 16870 (2016).

[9] M. Werinos, H. Antrekowitsch, T. Ebner, R. Prillhofer, P. J. Uggowitzer, and S. Pogatscher, Mater. Des. **107**, 257 (2016).

[10] D. J. Hepburn, E. MacLeod, and G. J. Ackland, Phys. Rev. B **92**, 014110 (2015).

[11] D. Terentyev, L. Malerba, and A. V. Barashev, Philos. Mag. Lett. **85**, 587 (2005).

[12] E. Vincent, C. S. Becquart, and C. Domain, J. Nucl. Mater. **351**, 88 (2006).

[13] D. Nguyen-Manh, A. P. Horsfield, and S. L. Dudarev, Phys. Rev. B **73**, 020101(R) (2006).

[14] A. F. Calder, D. J. Bacon, A. V. Barashev, and Yu. N. Osetsky, Philos. Mag. **90**, 863 (2010).

[15] C. S. Becquart and C. Domain, Metall. Mater. Trans. A **42**, 852 (2011).

[16] S. L. Dudarev, Annu. Rev. Mater. Res. **43**, 35 (2013).

[17] C. L. Fu, M. Krcmar, G. S. Painter, and X.-Q. Chen, Phys. Rev. Lett. **99**, 225502 (2007).

[18] P. Olsson, T. P. C. Klaver, and C. Domain, Phys. Rev. B **81**, 054102 (2010).

[19] O. I. Gorbatov, P. A. Korzhavyi, A. V. Ruban, B. Johansson, and Y. N. Gornostyrev, J. Nucl. Mater. **419**, 248 (2011).

[20] Y.-W. You, X.-S. Kong, X.-B. Wu, W. Liu, C. S. Liu, Q. F. Fang, J. L. Chen, G.-N. Luo, and Z. Wang, J. Nucl. Mater. **455**, 68 (2014).

[21] T. R. Mattsson and A. E. Mattsson, Phys. Rev. B **66**, 214110 (2002).

[22] D. E. Jiang and E. A. Carter, Phys. Rev. B **67**, 214103 (2003).

[23] C. Wolverton, Acta Mater. **55**, 5867 (2007).
[24] G. Rahman, I. G. Kim, H. K. D. H. Bhadeshia, and A. J. Freeman, Phys. Rev. B **81**, 184423 (2010).
[25] W. Xie, W. Xiong, C. A. Marianetti, and D. Morgan, Phys. Rev. B **88**, 235128 (2013).
[26] D. R. Olander, in *Fundamental Aspects of Nuclear Reactor Fuel Elements*, Technical information center, Energy research and development administration, U. S. Department of Energy (1976).
[27] K. Hack, J. Korb, and D. Neuschutz, in *The SGTE Casebook Thermodynamics at Work*, 2nd ed., edited by K. Hack (Woodhead Publishing Limited, Cambridge, England, 2008), p. 178.
[28] M. Neubauer, K. P. Lieb, P. Schaaf, and M. Uhrmacher, Phys. Rev. B **53**, 10237 (1996).
[29] S. Amirthapandian, B. K. Panigrahi, S. Rajagopalan, A. Gupta, K. G. M. Nair, A. K. Tyagi, and A. Narayanasamy, Phys. Rev. B **69**, 165411 (2004).
[30] B. Rauschenbach, A. Kolitsch, and K. Hohmuth, Phys. Status Solidi A **80**, 471 (1983).
[31] A. Kehrel, J. Keinonen, P. Haussalo, K. P. Lieb, and M. Uhrmacher, Radiat. Eff. Defects Solids **118**, 297 (1991).
[32] W. A. Counts, C. Wolverton, and R. Gibala, Acta Mater. **58**, 4730 (2010).
[33] D. H. R. Fors and G. Wahnstrom, Phys. Rev. B **77**, 132102 (2008)
[34] C. Domain, C. S. Becquart, and J. Foct, Phys. Rev. B **69**, 144112 (2004).
[35] A. F. Bialon, T. Hammerschmidt, and R. Drautz, Phys. Rev. B **87**, 104109 (2013).
[36] C. Barouh, T. Schuler, C.-C. Fu, and M. Nastar, Phys. Rev. B **90**, 054112 (2014).
[37] M. Souissi, Y. Chen, M. H. F. Sluiter, and H. Numakura, Comput. Mater. Sci. **124**, 249 (2016).
[38] C. Ravi, C. Wolverton, and V. Ozolins, Europhys. Lett. **73**, 719 (2006).
[39] ASM Alloy Phase Diagrams Database, P. Villars, editor-in-chief; H. Okamoto and K. Cenzual, section editors; http://www.asminternational.org, (ASM International, Materials Park, OH, 2016).
[40] P. Villars and L. D. Calvert, *Pearson's Handbook of Crystallographic Data for Intermetallic Phases*, 2nd ed. (ASM International, Materials Park, OH, 1991).
[41] PAULING FILE in: Inorganic Solid Phases, Springer Materials (Springer, Heidelberg, online database), edited by P. Villars.
[42] J. Sanchez, J. Fullea, C. Andrade, and P. L. de Andres, Phys. Rev. B **78**, 014113 (2008).
[43] D. Murali, M. Posselt, and M. Schiwarth, Phys. Rev. B **92**, 064103 (2015).
[44] G. Kresse and J. Hafner, Phys. Rev. B **47**, 558 (1993).
[45] G. Kresse and J. Furthmuller, Phys. Rev. B **54**, 11169 (1996).
[46] P. E. Blochl, Phys. Rev. B **50**, 17953 (1994).
[47] G. Kresse and D. Joubert, Phys. Rev. B **59**, 1758 (1999).
[48] J. P. Perdew, K. Burke, and M. Ernzerhof, Phys. Rev. Lett. **77**, 3865 (1996).
[49] M. Methfessel and A. T. Paxton, Phys. Rev. B **40**, 3616 (1989).
[50] C. Kittel, *Introduction to Solid State Physics*. 7th ed. (Wiley, New York, 1996).
[51] P. Soderlind, L. H. Yang, J. A. Moriarty, and J. M. Wills, Phys. Rev. B **61**, 2579 (2000).
[52] L. De Schepper, D. Segers, L. Dorikens-Vanpraet, M. Dorikens, G. Knuyt, L. M. Stals, and P. Moser, Phys. Rev. B **27**, 5257 (1983).
[53] E. Hayward and C.-C. Fu, Phys. Rev. B **87**, 174103 (2013).
[54] W. Counts, C. Wolverton, and R. Gibala, Acta Mater. **59**, 5812 (2011).
[55] C.-C. Fu and F. Willaime, Phys. Rev. B **72**, 064117 (2005).
[56] P. Zhang, J. Ding, D. Sun, and J. Zhao, J. Nucl. Mater. **492**, 134 (2017).
[57] L. Ventelon, B. Wirth, and C. Domain, J. Nucl. Mater. **351**, 119 (2006).
[58] Y. You, M. F. Yan, and H. T. Chen, Comput. Mater. Sci. **67**, 222 (2013).
[59] Y. Jiang, J. R. Smith, and G. R. Odette, Phys. Rev. B **79**, 064103 (2009).
[60] C. Liu, M. Asato, N. Fujima, and T. Hoshino, Mater. Trans. **54**, 1667 (2013).
[61] T. Ohnuma, N. Soneda, and M. Iwasawa, Acta Mater. **57**, 5947 (2009).
[62] R. A. Perez and M. Weissmann, J. Phys.: Condens. Matter **16**, 7033 (2004).
[63] X. Gai, R. Smith, and S. D. Kenny, J. Nucl. Mater. **470**, 84 (2016).
[64] J. P. Hirth, Metall. Trans. A **11**, 861 (1980).
[65] A. Jacob, E. Povoden-Karadeniz, and E. Kozeschnik, Calphad **60**, 16 (2018).
[66] H. Katsuraki and K. Suzuki, J. Appl. Phys. **36**, 1094 (1965).
[67] O. Kubaschewski, *Iron-Binary Phase Diagrams* (Springer-Verlag, Berlin, Heidelberg, 1982).
[68] H. W. King, J. Mater. Sci. **1**, 79 (1966).
[69] B. Drittler, N. Stefanou, S. Blugel, R. Zeller, and P. H. Dederichs, Phys. Rev. B **40**, 8203 (1989).
[70] H. K. D. H. Bhadeshia, J. Mater. Sci. **39**, 3949 (2004).
[71] X. Gai, T. Lazauskas, R. Smith, and S. D. Kenny, J. Nucl. Mater. **462**, 382 (2015).
[72] L. Messina, M. Nastar, T. Garnier, C. Domain, and P. Olsson, Phys. Rev. B **90**, 104203 (2014).
[73] L. Messina, M. Nastar, N. Sandberg, and P. Olsson, Phys. Rev. B **93**, 184302 (2016).
[74] G. E. Murch in *Phase Transformations in Materials*, edited by G. Kostorz (Wiley-VCH Verlag GmbH, Weinheim, 2001).
[75] S. L. Shang, H. Z. Fang, J. Wang, C. P. Guo, Y. Wang, P. D. Jablonski, Y. Du, and Z. K. Liu, Corros. Sci. **83**, 94 (2014).
[76] G. R. Odette, B. D. Wirth, D. J. Bacon, and N. M. Ghoniem, MRS Bull. **26**, 176 (2001).
[77] R. A. Arndt and A. C. Damask, Acta Metall. **12**, 341 (1964).
[78] A. Moslong, E. Albert, E. Recknagel, A. Weidinger, and P. Moser, Hyperfine Interact. **15/16**, 409 (1983).
[79] M. Doyama, Bull. Jpn. Inst. Met. **25**, 808 (1986).
[80] R. Idczak, R. Konieczny, and J. Chojcan, J. Appl. Phys. **115**, 103513 (2014).
[81] J. L. Bocquet, C. Barouh, and C. C. Fu, Phys. Rev. B **95**, 214108 (2017).
[82] H. W. King, J. Mater. Sci. **6**, 1157 (1971).
[83] W. L. Roth, Phys. Rev. **110**, 1333 (1958).
[84] D. S. Parker, Sci. Rep. **7**, 3388 (2017).
[85] P. J. Brown, J. Deportes, and B. Ouladdiaf, J. Phys: Condens. Matter **4**, 10015 (1992).

[86] A. Subedi and D. J. Singh, Phys. Rev. B **81**, 024422 (2010).
[87] L. Haggstrom, T. Ericsson, R. Wappling, and K. Chandra, Phys. Scr. **11**, 47 (1975).
[88] T. Yashiro, Y. Yamaguchi, S. Tomiyoshi, N. Kazama, and H. Watanabe, J. Phys. Soc. Jpn. **34**, 58 (1973).
[89] D. Cherian, S. Robler, C. Koz, A. A. Tsirlin, U. Schwarz, S. Wirth, and S. Elizabeth, J. Appl. Phys. **115**, 123912 (2014).
[90] P. Bodeker, A. Schreyer, and H. Zabel, Phys. Rev. B **59**, 9408 (1999).
[91] M. A. McGuire, Crystals **7**, 121 (2017).